A class of single and dual-frequency algorithms for rain-rate profiling from a spaceborne radar. Part II: Tests from airborne radar data

Paul Amayenc, Jean-Philippe Diguet, Mongi Marzoug, Toufik Tani

A Class of Single- and Dual-Frequency Algorithms for Rain-Rate Profiling from a Spaceborne Radar. Part II: Tests from Airborne Radar Measurements

PAUL AMAYENC, JEAN PHILIPPE DIGUET,* MONGI MARZOUG,† AND TAOUFIK TANI

Centre d'études des Environnements Terrestre et Planétaires, Issy-les-Moulineaux, France

(Manuscript received 22 December 1994, in final form 14 June 1994)

ABSTRACT

In Part I, four single-frequency (SF) algorithms and a dual-frequency (DF) algorithm for range profiling of the rain rate from a spaceborne radar were described and tested from numerical simulations. In Part II, performances of these algorithms are studied using data from a DF (X and K_a bands) near-nadir-pointing airborne radar. The data, gathered over ocean near Wallops Island in 1988, mimic future spaceborne radar measurements.

Rain retrievals are performed for isolated and series of contiguous rain measurements within stratiform and convective rain regions overflown by the aircraft. General features and aspects specific to the experiment conditions are pointed out. The SF algorithms provide more or less scattered results according to their own sensitivities to uncorrected scaling errors. Improvement of the algorithms stability by constraining the total path-integrated attenuation from surface echo measurements is confirmed. The correlation between attenuation coefficients at both frequencies, which forms the theoretical basis of the DF algorithm, is verified from the data. Results from DF algorithm are likely more reliable than SF counterparts since they are globally corrected for scaling errors. Rain-rate thresholds above which "attenuation" algorithms should relay Z–R methods to avoid negative bias in rain-rate estimates are found near 12 mm h^{-1} at X band and 1 mm h^{-1} at K_a band for a 2.5-km rain depth. Coherent spatial structures of the rain rate within a vertical cross section of the storm are recovered from the "attenuation" algorithms.

The data obtained with a cross-range resolution $L_0 \approx 1$ km are also used to perform 2D simulations of beam-averaging, and nonuniform beam-filling (NUBF) effects are used for cross-range resolutions $L = 2$, 3, and 4 km. Degrading the resolution produces a smoothing of small-scale rain-rate structures and a lowering of the rain-rate estimation. Bias due to NUBF depend on the involved "attenuation" algorithm. It increases with L but remains below 15%, up to $L = 4$ km for mean rain-rate estimates at large horizontal scale ($\approx$100 km). The Z–R methods are weakly affected by the NUBF.

1. Introduction

Spaceborne weather radar will play an important role for measuring rainfall from space in the near future (see, e.g., Meneghini and Kozu 1990). Elaborating methods for profiling the rain rate versus range from spaceborne radar measurements led us to define a class of single-frequency (SF) and dual-frequency (DF) algorithms in Part I of the present paper (Marzoug and Amayenc 1994, hereafter referred to as MA94). All the algorithms make use of a common mathematical formalism and perform correction for path-integrated attenuation (or PIA). The potential merit–demerit balance of the proposed algorithms were thoroughly discussed. Results of numerical simulations of algorithms performances using theoretical models of rain-rate profiles were also reported. In this paper, we present application of these algorithms to real data from airborne radar measurements.

Airborne experiments performing sampling of rainy systems from the top are useful to study rainfall retrieval methods. Since some years, an increasing number of airborne radar experiments at frequencies envisioned for future spaceborne measurements were conducted. The data were used in several studies (e.g., Fujita et al. 1985; Meneghini et al. 1989, 1992; Meneghini and Nakamura 1990; Marzoug and Amayenc 1991a, 1992, 1993; Kozu et al. 1991; Amayenc and Marzoug 1992; Iguchi and Meneghini 1994) to test a variety of algorithms envisioned for exploiting future spaceborne radar measurements. Here we used data of such a dedicated experiment.

The present paper rests on the content of Part I (MA94), which is assumed to be known by the reader. The same notations are used. In section 2, the foundings and the most striking features of the involved algorithms, as deriving from MA94, are briefly recalled. The origin and characteristics of the airborne radar data and the nature of the validation tests used to study the

* Current affiliation: LASTI/ENSSAT, Lannion, France.
† Current affiliation: CNET/PAA, Issy-les-Moulineaux, France.

Corresponding author address: Dr. Paul Amayenc, CETP-CNET, 38 rue du General Leclerc, 92131 Issy-les-Moulineaux, France.

algorithms performances are described in section 3. Then, in section 4, we present results of application of the range-profiling single- and double-frequency (SF and DF, respectively) algorithms to these data and tests of their performances. This is done while ignoring possible nonuniform beam-filling (NUBF) effects that may be a significant source of errors for low-beam-resolution measurements usually planned for spaceborne instruments. Simulations of NUBF effects using the airborne radar data are investigated in section 5. Conclusions are given in section 6. Mathematical development dealing with a method to evaluate the PIA over a limited range interval is given in the appendix.

2. Summary of algorithms characteristics

The SF algorithms are based upon the use of a $Z = \alpha k^{\beta}$ relation to derive the range-profiled attenuation coefficient further converted into a range-profiled rain rate by means of the $k = cR^{d}$ relationship. Four variants were defined correcting for various types of scaling errors, constant with range, possibly present in radar measurements. The *kZ* algorithm processing only rain echoes is, in essence, similar to the approach of Hitschfeld and Bordan (1954). It is sensitive to an offset in the radar calibration and to variability in the drop size distribution (DSD) and becomes rapidly unstable when PIA increases. Additional measurements of surface echo attenuation are used as a constraint in two out of four algorithms to correct for scaling errors. The *kZC* algorithm corrects for an offset δC in the radar calibration but is sensitive to error δA_t in σ^0 estimate, especially for low PIA, and to DSD variability. It also depends on storm structure along the entire path. The *kZS* algorithm corrects for any unknown PIA factor over a range interval $(0, r_0)$ prior to the first processed range gate at range r_0 by integrating from the surface; thus, it is insensitive to the storm structure at ranges less than r_0 within the cloud or melting region, for example. It remains, however, sensitive to errors δC and δA_t and to DSD variability. The *kZC* and *kZS* algorithms are generally stable, and the impact of uncorrected error terms decreases with the PIA amount. The fourth algorithm, *kZN*, assumes constant rain rate versus range within a limited range interval to estimate the attenuation coefficient $k_m(r_d)$ at range r_d near the surface; then upward integration of "rain signal" is performed to get the range-profile of the attenuation coefficient. It is insensitive to errors δC or δA_t and moderately sensitive to DSD variability. However, the presence of significant rain gradient versus range near r_d, due to evaporation process, for example, is a possible source of error. Since the four SF algorithms have complementary sensitivities to uncorrected scaling errors, intercomparison of the results was proposed as a means to identify the need for such corrections on individual basis.

The DF algorithm was conceived to improve the correction of scaling error terms possibly present in rain measurements. This is done by exploiting the relationship $k(f_2) = a(f_1, f_2)k(f_1)^b$ between the attenuation coefficients at two differently attenuating frequencies (with $f_2 > f_1$). The nonlinear regression process used to adjust the relation is initialized by means of the various pairs of range-profiled attenuation coefficients provided by the SF algorithms at both frequencies and performs the best fit. Accordingly, the DF algorithm output provides two estimates of the rain-rate profile, one for each frequency. The closeness of these two estimates is a necessary, though not sufficient, condition to assess the credibility of the solution. No explicit use of surface echo measurements is made except in part of the initialization process, implying results of *kZC* and *kZS* algorithms. The DF approach is more efficient than SF counterparts since it removes scaling errors not corrected in SF algorithms. It also adjusts the DSD-dependent parameters of the rain relations used in the analysis from the initial adjustment of the a parameter in the $k(f_2)-k(f_1)$ relation. Besides, the DF algorithm still works when, for large PIA, the rain signal for the most attenuating frequency f_2 falls below noise level before the surface range.

3. Data from airborne radar experiment

a. Data selection

During past years, CRL (Communications Research Laboratory, Tokyo) and NASA/GSFC have been conducting a series of joint aircraft experiments using the microwave airborne rain scatterometer/radiometer (MARS) developed at CRL. This "integrated" instrument, originally developed in 1979 (Okamoto et al. 1982) and further improved, includes a downward-looking DF (10.00 and 34.45 GHz) radar and a DF (9.86 and 34.21 GHz) radiometer. We did not consider measurements in the radiometer mode.

In the 1988–89 experiment, a series of flights with the NASA T-39 Sabreliner jet plane were conducted near Wallops Island, mainly over Chesapeake Bay. The flight altitude, above 10-km altitude, allowed simulation of spacelike observations and examination of heavier convective storms and the upper structure of the precipitation. Most details on the experiment may be found in Kozu (1991), Kozu et al. (1991), and Meneghini et al. (1992). The quality of all datasets was guaranted by eliminating undesirable observations such those corrupted by radio interferences or taken during aircraft attitude fluctuations or banking. We selected the dataset obtained on 1 November 1988 flight as the most interesting one because it included observation of well-organized stratiform and convective rain areas with low to heavy rain. The aircraft flew northeast of Wallops Flight Facility (WWF/NASA) over the ocean between 1945 and 2230 UTC. At WFF, the altitude of 0°C isotherm was about 3 km, and the surface temperature was close to 11°C.

TABLE 1. Major system parameters for the dual-frequency radar onboard T-39 aircraft (adapted from Kozu 1991).

Parameter	X band	K_a band
Center frequency	10.00 GHz	34.45 GHz
Antenna		
Type	Horn lens	Horn lens
Polarization	Linear VV	Linear VV
Aperture	42 cm	13 cm
Gain	30.3 dB	30.4 dB
Half-power beamwidth	5.2°	5.2°
Scanning angle	Approx. nadir pointing	Approx. nadir pointing
Transmitter		
Peak power	20 kW	10 kW
PRF	440 Hz	440 Hz
Pulse width	0.5 μs	0.5 μs
Receiver		
Noise figure	5.3 dB	9.6 dB
Detection	Logarithmic	Logarithmic
Dynamic range	80 dB	80 dB
Signal processor		
Sample interval	0.2 μs	0.2 μs
Range window	22.5 km	20.25 km
No. of independent samples (nominal)	128	128

b. *Experiment conditions and data processing*

The main system parameters for the dual-frequency radar are listed in Table 1. The nominal cruising altitude of the aircraft was 11–12 km, with the X- and K_a-band antennas maintained fixed at near-nadir incidence. In fact, the mean incidence was generally very close to 5° off nadir, due to aircraft attitude. Thus, the range-gated measurements combined with aircraft motion yielded almost vertical cross section of the overflown precipitating systems.

The nearly identical half-power beamwidths of about 5° provide a 1-km surface footprint and well-matched observation volumes within precipitation at both frequencies. Note that the 3-dB footprint actually corresponds to 6-dB beamwidth because the antenna gain function is applied for both transmission and reception. The small footprint size allows us to consider that NUBF effects are almost negligible. The nominal cruising speed of the aircraft is about 200 m s^{-1}. Each radar observation for an entire path, enabling observation of rain, surface, and mirror echoes within the range window, consists of a 128-sample average over approximately 0.4 s, which corresponds to a horizontal displacement of the aircraft of about 80 m. With 1-km footprint, there is a large overlap of radar beams from one observation to the next one. Independent measurements for contiguous footprints are actually obtained every 4.8 s, or every 12 observations. One minute of data, or 150 observations, corresponds to an "equivalent" horizontal length of about 12 km if observation is continuous.

Special care was taken by the experimenters to perform accurate radar calibration. The method included internal calibration using calibrated signal and noise sources, external calibration process using radar measurements at X band for an over–rain gauge flight above land, and adjustments of radar return powers at X and K_a bands from small ice scatterers above the bright band during light stratiform rain. Details and results may be found in Kozu (1991) and Kozu et al. (1991).

The mean returned power measurements within rain were first corrected by subtracting the mean noise power estimated within "no rain" gates along the path, then converted into reflectivity factors by means of the calibration procedure provided by the experimenters. The pulse duration of 0.5 μs at each frequency provided a nominal range resolution of 75 m. The return pulse, however, was oversampled at a 5-MHz rate, that is, a 0.2-μs interval or 30 m. Thus, reflectivities data were generated over contiguous 75-m gated intervals by us-

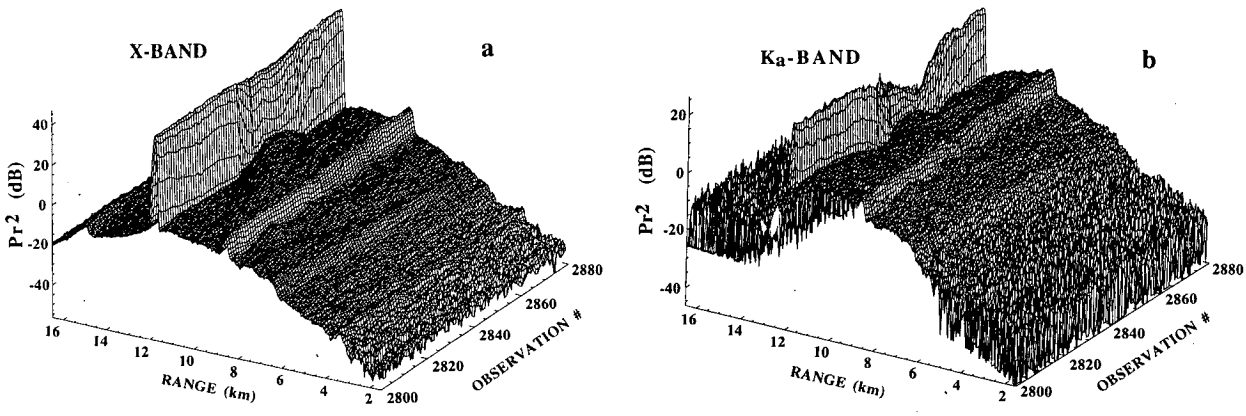

FIG. 1. Example of 3D plot of selected profiles of range-normalized mean received power Pr^2 (in arbitrary decibels) in the 1.5–16.5-km range interval (a) at X band and (b) at K_a band for the 1 November 1988 experiment over ocean. The sequential observation number ranges from 2800 to 2880.

ing weighted running means of the genuine data. The minimum detectable "apparent" reflectivity factor next to the surface (11-km range) was about 15 dBZ at both frequencies.

Figure 1 shows an example of 3D plots of the mean received power profile normalized to squared range r^2 for an ensemble of 81 contiguous observations (see Fig. 3) at X band and K_a band in the 1.5–16.5-km range interval. The large peak at about 11.2-km range is the surface return. At X band, the surface return is almost constant indicating low PIA. At K_a band, larger PIA is evident from variations in the surface return. The K_a-band signal is largely contaminated by noise near aircraft and deep in the rain. Below the surface, the mirror image return is present at X band, while it disappears at K_a band. A brightband, less pronounced at K_a band than at X band, is present near range 8.2 km. Figure 2 shows a 3D plot of the difference between "apparent" rain reflectivities factors at both frequencies: $\Delta Z = Z_{m,X} - Z_{m,K}$.[1] The plot is limited to the range interval 5–11 km. From low to large ranges, ΔZ shows first a chaotic region dominated by noise effects, then a peak near range 8.2 km due to difference in the brightband magnitudes at both frequencies, and finally a monotonic increase due to growing differential path-attenuation.

The surface echo power measurements were processed to get "apparent" values σ^0_m of the surface backscatter coefficient below rain. At X band, the surface echo was always found detectable, even for heavy rain, and σ^0_m was computed from the observed peak value of the surface return. At K_a band, σ^0_m was determined in the same manner when surface return was detected. For heavy rain, however, when the surface return was masked by noise, σ^0_m was computed using the noise level at the surface range. Obviously, this underestimated the total PIA in the rain layer. For each frequency, the reference value of σ^0 outside rainy areas was also determined (see section 4a).

c. *Nature of the validation tests*

As most experiments with T-39 in 1988–89, the selected experiment did not involve permanent means, such as rain gauge networks or ground-based radars, enabling "external" validation of the rain structures retrieved from the various algorithms. This came mainly from the fact that the overflown rainy areas were most frequently located over ocean, too far from the ground-based SPANDAR radar in operation at WFF or from existing land-based rain gauges. Thus, we had to conceive "internal" procedures to validate results of aircraft radar. The basic step was to compare rain profiles recovered from every algorithm at X band and K_a band, since the involved PIA effects corrected by the algorithms are different (cf. Table 3). These comparisons were studied for selected profiles or for series of contiguous profiles. In the latter case, we used mean rain rates over the rain-layer depth, derived from profiles retrieved from various algorithms. We also analyzed reconstructed 2D rain structures within the vertical alongtrack plane. Besides, interpretation of the experimental results profited by significant inputs from theoretical simulation results (e.g., Marzoug and Amayenc 1991b; MA94).

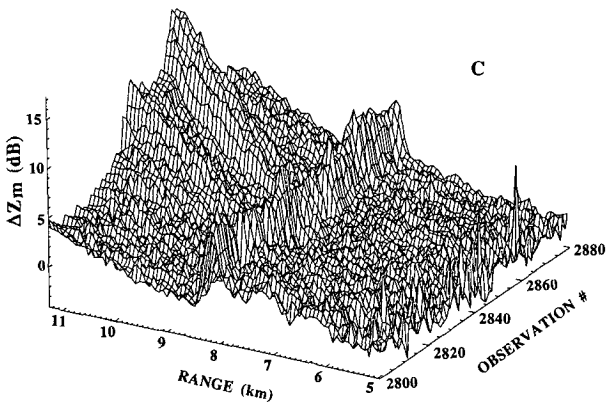

FIG. 2. Example of 3D plot of the difference $\Delta Z_m = Z_{m,X} - Z_{m,K}$ (dB) between the apparent rain reflectivity factors at both frequencies. The sequential observations ranging from 2800 to 2880 are the same as in Fig. 1.

4. Application of SF and DF algorithms: Results and discussion

a. *Algorithms processing*

Some specific aspects of the algorithms processing rounding off the general description given in MA94 and the elements given in section 2 are hereafter made clear.

To process *kZC* and *kZS* algorithms, the model of σ^0 outside rain was determined by processing surface returns in clear areas as close as possible to the raining areas observed during the flight. Data were first ranked according to the beam incidence, within angular intervals of 2° centered from 3° to 9°, then averaged within each angular interval. For the most frequent incidence, near 5°, involving about 1150 data points, the mean value was $\langle \sigma^0 \rangle \approx 1.8$ dB (4.2 dB), with a standard deviation of 0.5 dB (1.4 dB) at X band (K_a band).

For cases where rain signal was obscured by noise in the range interval (r_d, r_s), as commonly observed for large PIA at K_a band, a procedure assuming constant rain rate in this interval to correct for the unknown PIA factor $A(r_d, r_s)$ was included in *kZC* and *kZS* algorithms (MA94).

The slope technique, used in the kZN algorithm to determine $k_m(r_d)$, was applied over four contiguous

[1] In the following, subscripts X and K stand for X band and K_a band, respectively.

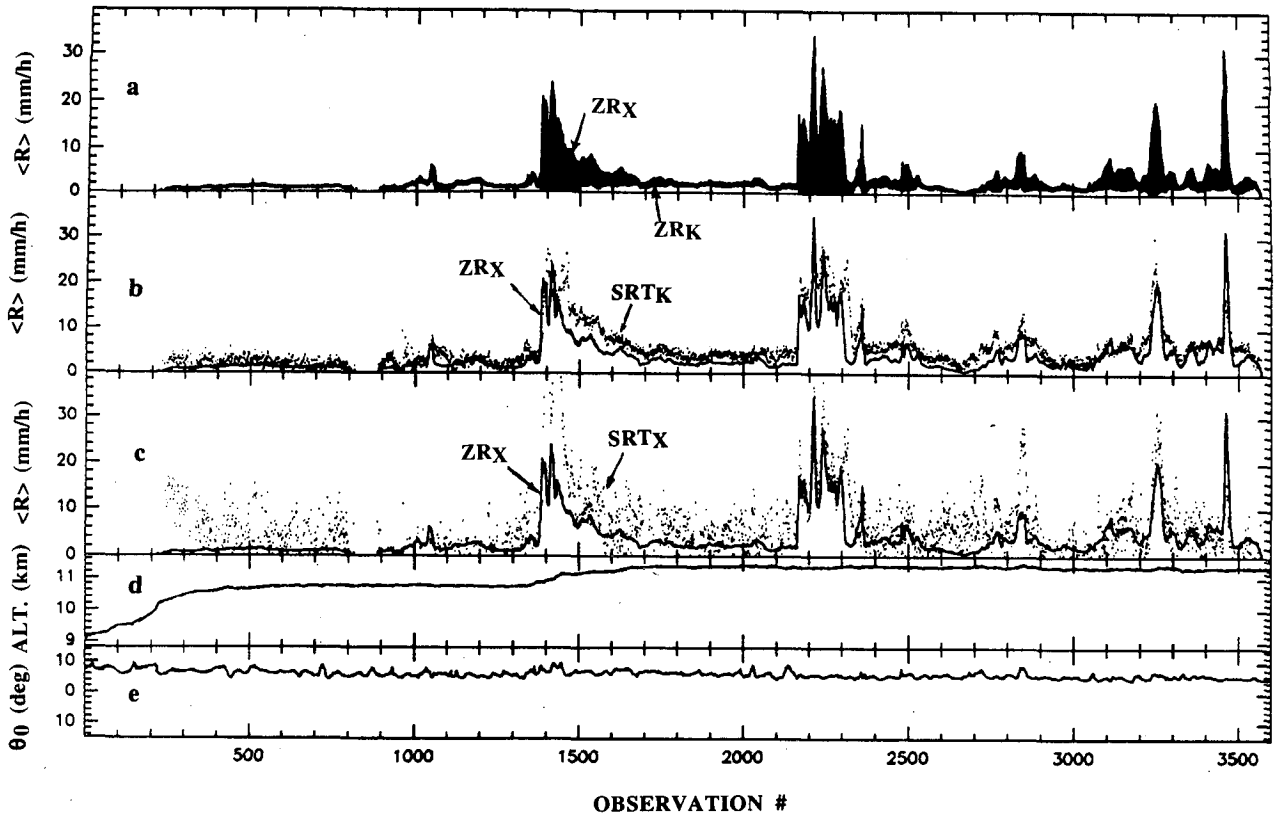

FIG. 3. Display of several parameters for increasing observation numbers derived from the dataset on 1 November 1988. The panels show (a) the mean (layer-averaged) rain rates $\langle R_X \rangle$ ($\langle R_K \rangle$) computed from the backscatter method at X band (K_a band) using the ZR_X (ZR_K) relationship (the dashed area points out difference between the two estimates); (b) the mean (layer-averaged) rain rate from SRT_K (dots) compared with $\langle R_X \rangle$ (full line); (c) the mean (layer-averaged) rain rate from SRT_X (dots) compared with $\langle R_X \rangle$ (full line); (d) the aircraft flight altitude above MSL; (e) the off-nadir incidence of the radar beam. Note that 100 contiguous observations (gathered during about 40 s) are equivalent to a horizontal distance of about 8 km.

gates where SNR > 3 dB near range r_d, the closest as possible to the surface range r_s.

For DF algorithm, an automatic procedure was used to identify the r_1-r_2 range interval where difference in rain reflectivities at both frequencies increased monotonically versus range, enabling exploitation of the differential path-attenuation effect (see Fig. 2). Possible difference in the brightband region, where differences in reflectivity may result from non-Rayleigh scattering rather than differential path attenuation, was excluded.

TABLE 2. Relations between the integrated rainfall parameters [with Z in its usual units ($mm^6\ m^{-3}$), k in decibels per kilometer, and R in millimeters per hour] used in the algorithms to process the airborne radar data at X band and K_a band.

Relation	X band (10 GHz)	K_a band (35 GHz)
$Z-R$	$Z_X = 204R^{1.6}$	$Z_K = 314R^{1.3}$
$k-R$	$k_X = 0.014R^{1.136}$	$k_K = 0.219R^{1.047}$
$Z-k$	$Z_X = 8.315 \times 10^4\ k_X^{1.408}$	$Z_K = 2.09 \times 10^3\ k_K^{1.247}$
$k-k$	$k_K = 11.6k_X^{0.92}$	

The r_1-r_2 interval was required to include at least five contiguous range gates, with detectable rain signals (SNR ≥ 3 dB) at both frequencies.

The relations between the integrated rain parameters Z, k, and R, used to run the algorithms, are listed in Table 2. They are similar to those used in previous studies (e.g., Kozu 1991; Kozu et al. 1991; Meneghini et al. 1992) dealing with tests of rain retrieval algorithms from similar data. The $Z-R$ and $k-R$ relations are taken from Atlas and Ulbrich (1977), who used Mie calculation and power-law fits to a set of measured drop size distributions, except the Z_X-R law based on the DSD model of Marshall and Palmer (1948). The $Z_{X,K}-k$ relations used in SF algorithms, and the k_K-k_X relation used in DF algorithm, are derived from them.

It is helpful to indicate the expected PIA as a function of rain rate and frequency. This is given in Table 3 using $k-R$ laws of Table 2 with constant rain rate $\langle R \rangle$ over a 3-km rain depth. For completeness, a PIA of 3 dB (10 dB) is produced by $\langle R_X \rangle = 23.3$ mm h^{-1} (67.3 mm h^{-1}) and $\langle R_K \rangle = 2.2$ mm h^{-1} (7 mm h^{-1}). Note that the PIA exceeds the observed standard de-

TABLE 3. Expected values of the total two-way PIA at X band (PIA_X) and K_a band (PIA_K) over a 3-km-deep rain layer with uniform rain rate $\langle R \rangle$ using $k-R$ relations in Table 2.

$\langle R \rangle$ (mm h^{-1})	1	2	5	10	20	40
PIA_X (dB)	0.08	0.18	0.53	1.15	2.52	5.55
PIA_K (dB)	1.31	2.72	7.09	14.6	30.3	62.5

viation in σ^0 estimate for $\langle R_X \rangle$ above 6 mm h^{-1} and $\langle R_K \rangle$ above 1.1 mm h^{-1}. For rain rates below these values, uncertainties in σ^0 estimates may have significant impact on the accuracy of path-averaged rain rates deduced from the surface reference technique (or SRT), as shown by Meneghini et al. (1992).

b. *Overview of attenuation effects*

The selected dataset includes 3600 observations. Several parameters characterizing these observations are displayed in Fig. 3. The aircraft altitude flight, shown in Fig. 3d, slowly varies from 9.2 to 11.4 km. The off-nadir incidence of the radar beam, shown in Fig. 3e, ranges between 4° and 10°, and most frequently in the 5°–6° angular interval. Estimates of the mean layer-averaged rain rate $\langle R_X \rangle$ and $\langle R_K \rangle$ are shown in Fig. 3a. They were obtained by using Z_X-R and Z_K-R relations (cf. Table 2) to get R profile from apparent reflectivity Z_m above a 15-dBZ threshold, then averaging versus height. At X band, where PIA effects remain moderate, $\langle R_X \rangle$ points out rather well the mean rain-rate structure. Several zones of heavy rain are observed near observations 1400, 2200, 3250, and 3450. Though possibly affected by uncorrected PIA effects for moderate to heavy rain, the $\langle R_X \rangle$ estimate may be taken as a reference for comparison to characterize stronger attenuation effects at K_a band. Here $\langle R_K \rangle$ agrees with $\langle R_X \rangle$ for low rain rates only ($\leq$2 mm h^{-1}, typically). Above this threshold, attenuation at K_a band produces increasingly negative bias in $\langle R_K \rangle$, and "saturation" effect occurs. Meneghini et al. (1989) gave theoretical estimation of the saturation threshold in $\langle R_K \rangle$ estimate using a uniform rain model, in agreement with the observations. The path-averaged rain rate estimated from surface echo attenuation using SRT_K (SRT_X) is compared with $\langle R_X \rangle$ in Fig. 3b (Fig. 3c). The SRT_K estimate, which is not too affected by uncertainties in σ^0 estimates owing to large PIA at K_a band, is in fair agreement with $\langle R_X \rangle$. Conversely, large scatter and strong deviations from $\langle R_X \rangle$ are observed in SRT_X estimate. This occurs when the PIA and the mean error in σ^0 are of the same order of magnitude (cf. Table 3): the SRT_X may even produce meaningless "negative" rain-rate estimates (not plotted in Fig. 3c). Meneghini et al. (1987, 1992) have shown that a dual-frequency version of the SRT improved the path-averaged rain estimates by reducing the impact of uncertainties in σ^0.

We searched for an experimental verification of the k_K-k_X relation between attenuations at both frequencies, which constitutes the theoretical basis of the DF algorithm. For this purpose, we used estimates of the two-way PIA factor $A(r, r_s)$ at X and K_a bands derived from MA94, and we made this clear in the appendix. Neglecting uncorrected error terms in (A4) yields

$$A(r, r_s) = \left[1 + \left(\frac{0.46}{\beta}\right) \times (A_{tm}\alpha)^{-1/\beta} \int_r^{r_s} Z_{am}^{1/\beta}(r)ds\right]^{-\beta}, \quad (1)$$

where A_{tm} is the "measured" surface echo two-way attenuation factor, $Z_m(r)$ is the apparent rain reflectivity at range r, and r_s is the surface range.

The PIA factors were calculated over the range interval (r, r_s) covering the first 2 km above the surface, and then used to determine the correlation between the mean attenuation coefficients at both frequencies. The results are shown in Fig. 4. The "experimental" power-law best fit deriving from 2801 observations (i.e., 800 to 3600) is

$$k_K = 10.54k_X^{0.775}, \quad (2)$$

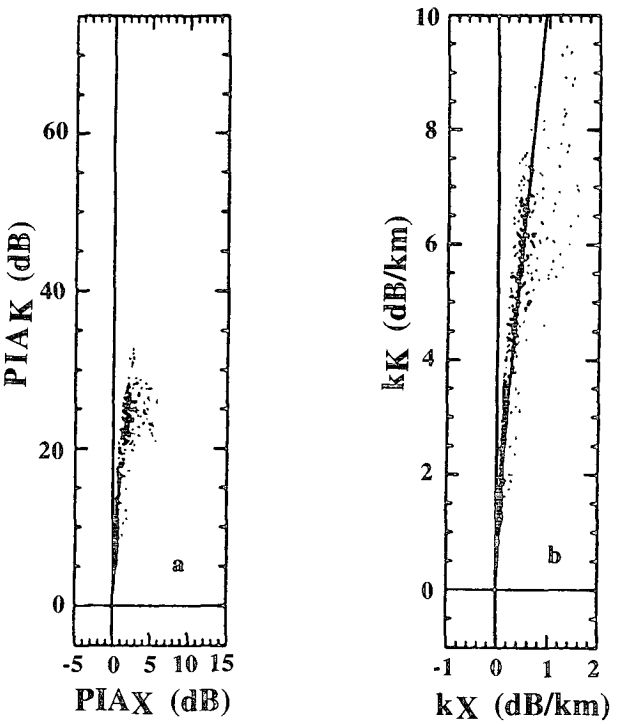

FIG. 4. Overall attenuation effects computed from 2801 data pairs (observations 800–3600 on 1 November 1988): (a) scatterplot of the two-way PIA at K_a band versus X band integrated over the first 2 km (above the surface) of the rain layer; (b) corresponding mean specific attenuation coefficients (dB km^{-1}) at K_a band versus X band and best power-law fit to the results.

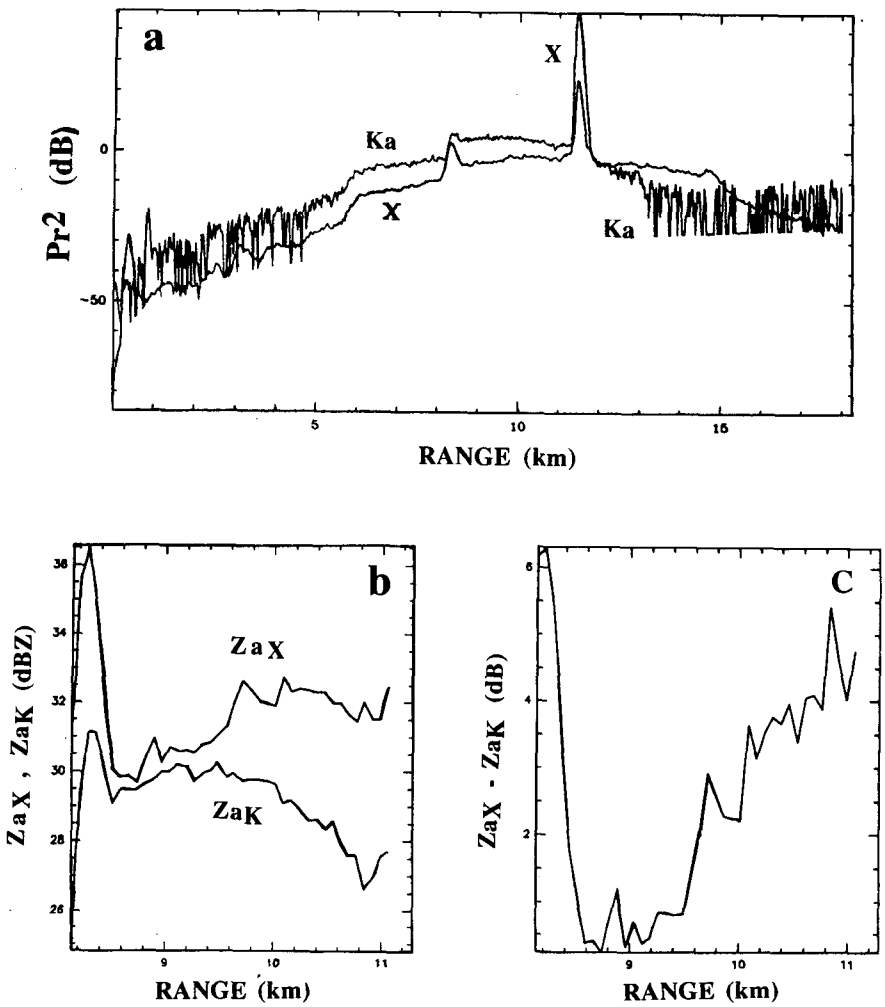

FIG. 5. Example of radar measurements within stratiform rain (observation 2821, off-nadir beam incidence 6.1°). Range-profiles of (a) range-normalized received powers Pr^2, (b) apparent reflectivities Z_X and Z_K, and (c) the difference in apparent reflectivity ($Z_X - Z_K$) at X and K_a bands.

with a high value of the correlation coefficient, $\rho = 0.996$.

This "experimental" law compares rather well with the selected "empirical" law (see Table 2):

$$k_K = 11.2k_X^{0.92}. \quad (3)$$

When total PIA provided by measurements of surface echo attenuation are used for the same purpose, the obtained experimental law, $k_K = 5.40k_X^{0.545}$ with $\rho = 0.712$, worsens. This comes from uncertainties in the PIA (see Fig. 3) for low rain rates that are also responsible for occasional nonphysical "negative" values. Conversely, (1) always yields positive PIA estimates, though it is still sensitive to errors in σ^0 (see the appendix). We also verified that (2) was not too much affected by uncertainties in α coefficient of the $Z = \alpha k^\beta$ relation at each frequency. The obtained a (b) parameter in the $k_K = ak_X^b$ relation varied from 9.1 to 11.5 (0.72 to 0.92) for ±50% changes in α, while ρ (≥ 0.96) remained very high.

For running the DF algorithm, however, we used (3) (cf. Table 2) instead of the "experimental" law (2) in order to preserve a full coherency between all relations involved in the analysis. Let us be reminded, however, that the parameter a is adjusted in the DF algorithm processing (MA94).

c. *Selected results for isolated rain profile retrievals*

The study is now focused on the data subset covering observations 2000–3600, which includes low to heavy rain-rate cases. The 1601 observations in question correspond to an acquisition time of 640 s, or about 128 km along track, within the rainy system. Two typical examples of the isolated rain-rate profile retrieved from SF and DF algorithms for stratiform and convective precipitation are presented below.

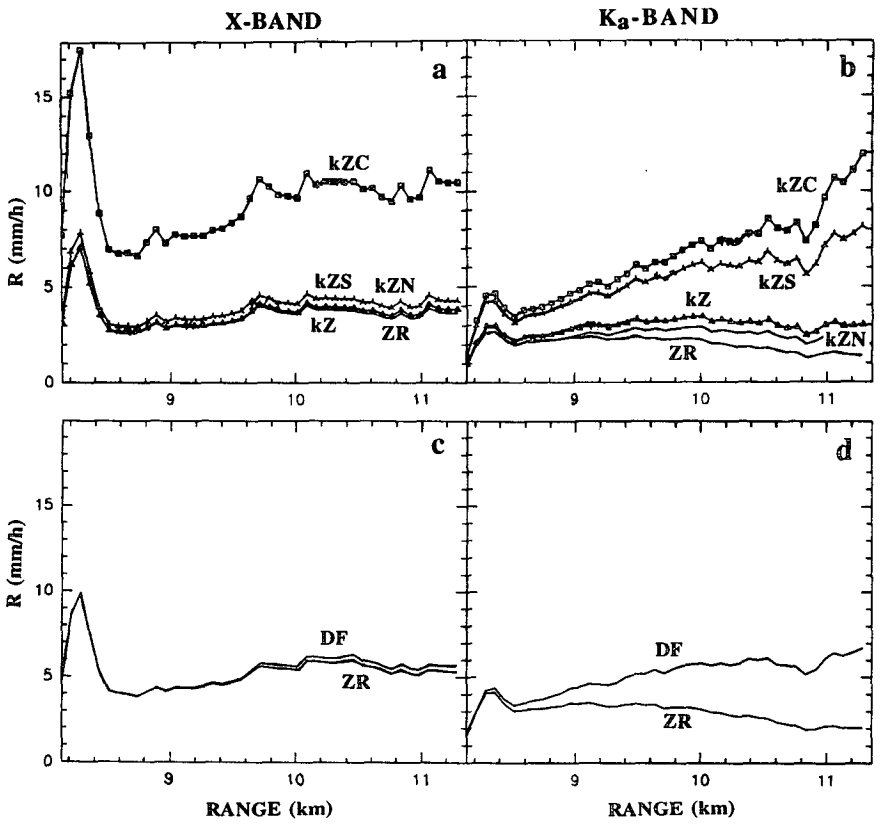

FIG. 6. Example of range-profiled rain rates within stratiform rain (observation 2821, off-nadir beam incidence 6.1°) retrieved from the SF algorithms and the Z–R algorithm (a) at X band and (b) at K_a band, and from the DF algorithm and the "corrected" Z^{cor}–R algorithm (c) at X band and (d) at K_a band. See radar measurements in Fig. 5.

The first example corresponds to observation 2821 (see Fig. 3) in stratiform rain with low rain rate. In Fig. 5 the range-normalized rain powers are plotted, along with the derived apparent reflectivities at both frequencies and their difference $\Delta Z = Z_X - Z_K$ over the last 3-km range interval. The brightband peak, more pronounced at X band than at K_a band, is seen near range 8.3 km. In Fig. 5a, the peak is also seen in mirror image at X band near range 14.6 km, while signal at K_a band is obscured by noise beyond range 13 km. Below the bright band, ΔZ increases monotonically from 0 dB near range 8.6 km to 4 dB near the surface, while ignoring Rayleigh fluctuations.

In Fig. 6, the upper plots show the results for SF and Z–R algorithms. At X band, where $PIA_X = 1.2$ dB, the *kZ*-, *kZS*-, and *kZN* algorithm results are almost identical and close to the Z–R estimate ($\langle R \rangle \approx 4$ mm h^{-1} below the bright band). Here kZC_X yields high value ($\langle R \rangle \approx 10$ mm h^{-1}) likely due to high sensitivity to uncertainty in PIA estimate for such a low rain rate. At K_a band, where $PIA_K = 10.2$ dB, the Z–R algorithm obviously underestimates the rain rate. Here kZ_K and kZN_K, which do not use surface echo, produce almost similar low-attenuation correction, and their results ($\langle R \rangle \approx 3$ mm h^{-1}) are close to those obtained at X band; kZC_K and kZS_K, which use surface echo, both overestimate the attenuation correction. It was verified that a lowering of 0.7 dB in PIA_X and of 1.9 dB in PIA_K, slightly in excess of σ^0 uncertainties, could put results of kZC_X, kZC_K, and kZS_K in good accordance with those of other "attenuation" algorithms.

In Fig. 6, the lower plots show the two R profiles provided by the DF algorithm at X band and at K_a band, respectively, along with the Z–R estimate for each case. Here, however, the plotted Z_X^{cor}–R, and Z^{cor}–R estimates[2] were corrected for "calibration errors" in Z_X or Z_K derived from the DF algorithm (see MA94). They slightly differ from the genuine ZR_X and ZR_K results shown in upper panels. The two R profiles for the DF algorithm are in excellent agreement ($\langle R \rangle \approx 5$ mm h^{-1} below the bright band). Comparing with the Z_K^{cor}–R results at each frequency points out credible corrections of PIA effects.

[2] Superscript "cor" stands for the involved correction of Z–R estimate.

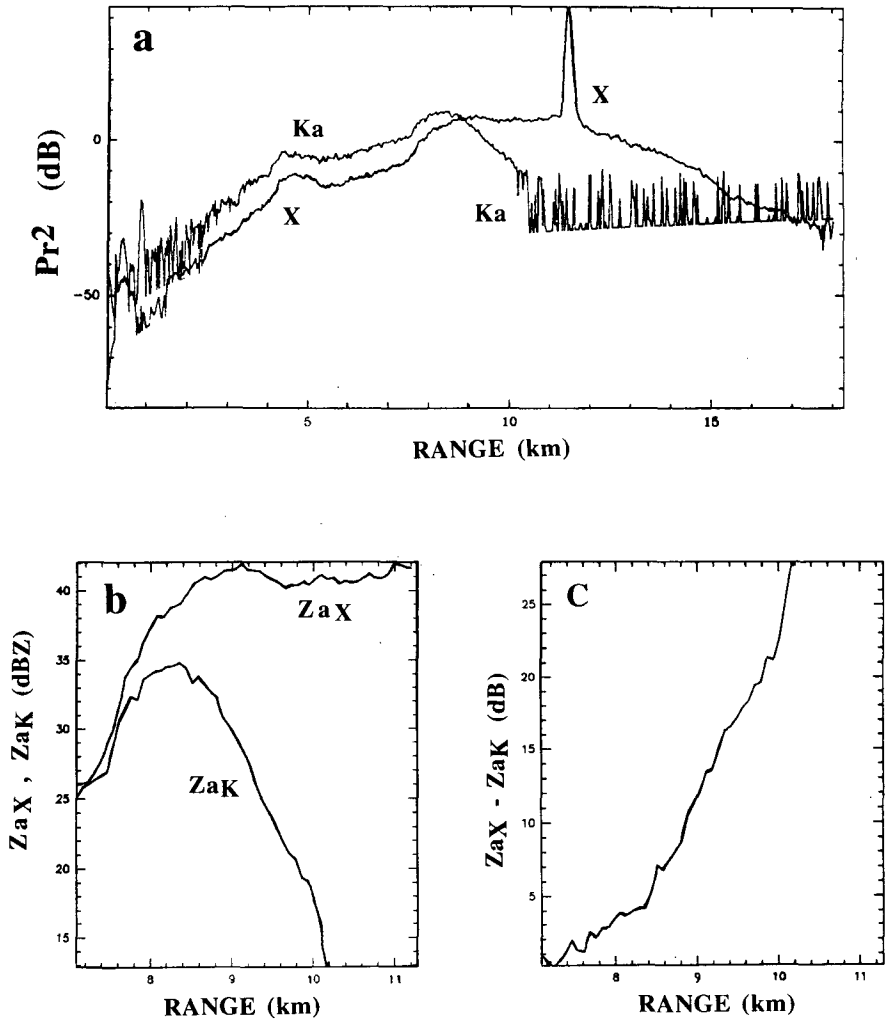

FIG. 7. Same as in Fig. 5 but for radar measurements within convective rain (observation 2233, off-nadir beam incidence 6°).

The second example corresponding to observation 2233 in convective rain with high rain rate is displayed in Fig. 7. The range-normalized rain powers and the derived apparent reflectivities at both frequencies do not reveal the presence of bright band. At K_a band, rain signal falls below noise at ranges beyond 10.2 km, and the surface echo is not detected. The difference between both reflectivities increases up to 28 dB in the detection range. Results for the SF and DF algorithms are shown in Fig. 8. Compared with previous results for stratiform rain, the SF algorithm results (upper panels) point out the increase in attenuation effects: $PIA_X \approx 3.8$ dB and $PIA_K > 40$ dB. At X band, results for the various "attenuation" algorithms are scattered within a margin of about 50% near the surface. At K_a band, kZ algorithm results, close to $Z-R$ estimate, strongly underestimate the R profile, while the nearly identical results for kZC_K and kZS_K algorithms diverge at low SNR near range 10 km. The kZN_K algorithm yields intermediate results. Corrections of scaling errors that could conciliate R profiles from "attenuation" algorithms at X and K_a band are approximately -1.2 dB for PIA_X in kZC_X and kZS_X and -2.3 dB for the radar "calibration" in kZ_K. Conversely, the two R profile estimates produced by the DF algorithm are very similar over the common range interval where both rain signals are detected and are not affected by the detection limit at K_a band. The $Z^{cor}-R$ results, at each frequency, are different by a factor up to 2 from those of the genuine $Z-R$ relations. In absence of such corrections, attenuation effects would appear unrealistically large, especially at X band.

d. Statistical tests and 2D rain structures from an ensemble of rain profiles

We characterized the overall quality of the rain rates recovered from various algorithms by comparing the

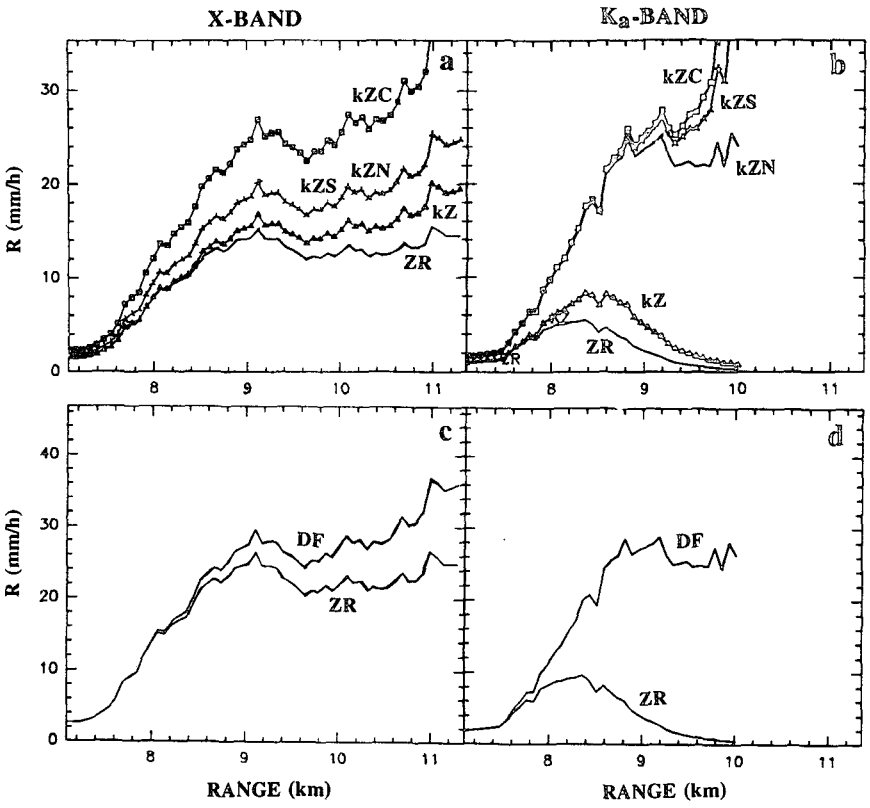

FIG. 8. Same as in Fig. 6 but for range-profiled rain rates retrieved within convective rain (observation 2233, off-nadir beam incidence 6.1°). See radar measurements in Fig. 7.

height-averaged rain rates computed from the 1601 R profiles of the dataset. For saving internal coherency of the results for stratiform and convective precipitation, the height-average $\langle R \rangle$ of the R profiles was performed over the first 2.5 km above the surface, that is, within rain below the melting region. The results presented below are focused on kZS, DF, and $Z-R$ algorithms.

The results for kZS and $Z-R$ algorithms are displayed in Fig. 9. At X band, the two estimates are close to each other except for high rain rate where attenuation effects becomes significant. The kZS_K algorithm performs large corrections of PIA effects, while ZR_K "saturates" above about 2 mm h^{-1}. Results for kZS_X and kZS_K are fairly close to each other, which points out the capability of the kZS algorithm to correct for "attenuation" effects within a large dynamic range. The convergence of kZS algorithm results toward ZR_X estimates is well observed for low attenuations, that is, $\langle R \rangle$ below 10 mm h^{-1}. At K_a band, kZS_K and ZR_K are close to each other for $\langle R \rangle$ below 2 mm h^{-1} only.

The same kind of results, but for the kZS and kZ algorithms results, are displayed in Fig. 10. At X band, the two estimates are very close to each other. Differences between kZS_X and kZ_X are generally smaller than between kZS_X and ZR_X (see Fig. 9). Conversely, kZ_K produces unstable results that generally underestimate the rain rate except near observation 2270 where a local overestimation effect is observed. This confirms that kZ algorithm corrects almost adequately low PIA effects (<3 dB) but fails to correct large PIA effects (>3 dB); it again points out the benefit of using surface echo as a constraint to improve the results.

The two rain estimates derived from the DF algorithm, at X band and at K_a band, along with the mean rain rates using $Z^{cor}-R$ relations at each frequency, are plotted in Fig. 11. We could verify that some isolated spikes were due to "bad" convergence of the DF algorithm. They correspond to cases where the required relative minimum of the functional used to adjust the $k(f_2)-k(f_1)$ relation in the nonlinear regression process (MA94) was very flat, or not even found. This happened for about 5% of the cases, especially for high rain rates. The general behaviors of the results from the DF algorithm and the kZS algorithm (shown in Fig. 9) are similar, despite some differences observed in the magnitudes of rain peaks. Also, the mean rain rates estimated either from the genuine ZR_X (ZR_K) relation or from the "corrected" $Z_X^{cor}-R$ ($Z_K^{cor}-R$) relation may be different. This is the case at X band, near observations 3150–3200 and 3350, where $Z-R$, in contrast to $Z_X^{cor}-R$, produces questionable higher $\langle R \rangle$ estimates than DF algorithm. In Fig. 12 the two $\langle R \rangle$ es-

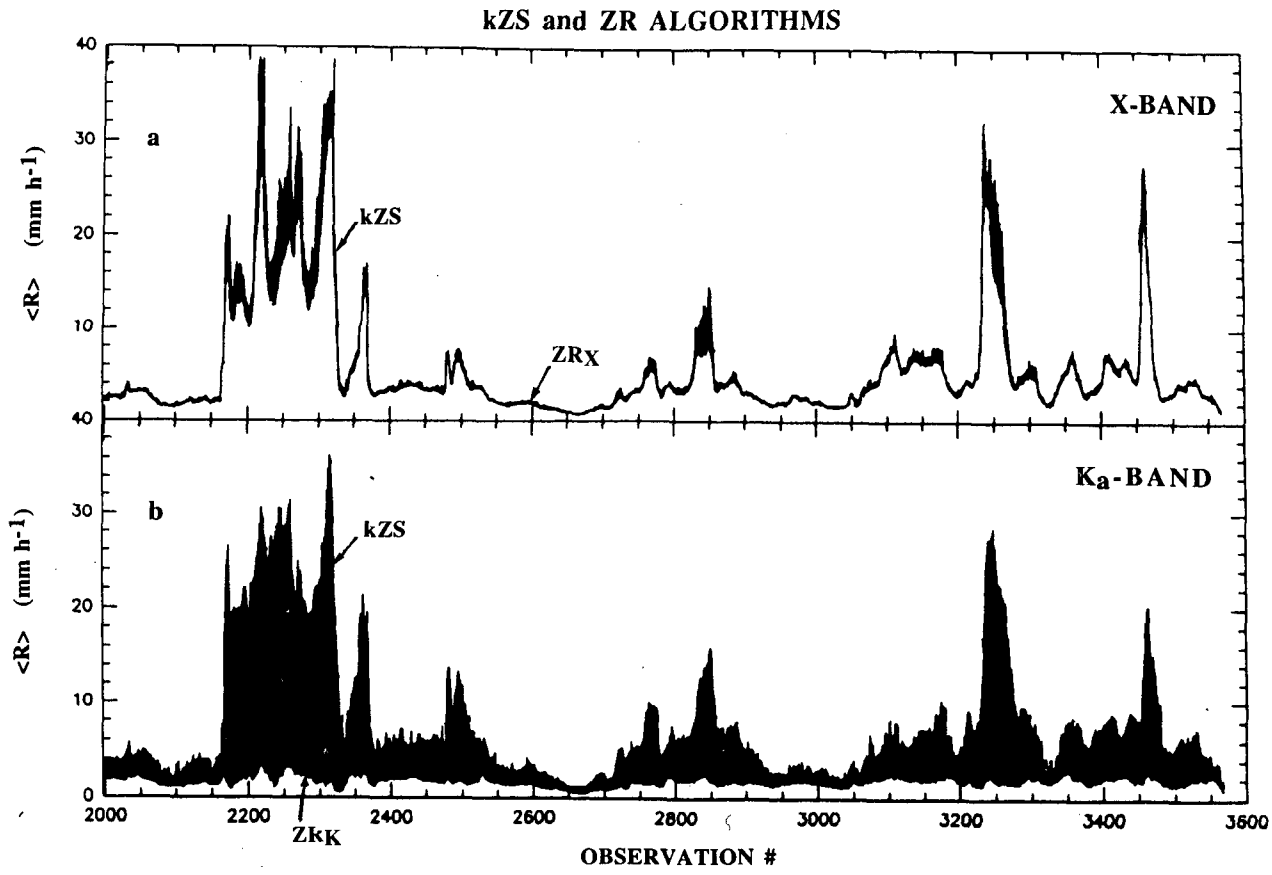

FIG. 9. Mean rain rates $\langle R \rangle$ (average over a 2.5-km depth above the surface) computed from 1601 R profiles (observations 2000–3600 on 1 November 1988) retrieved from kZS and Z–R algorithms (a) at X band and (b) at K_a band. For each panel, a positive (negative) difference between the kZS- and Z–R algorithms results is characterized by a black (blank) area.

timates from the DF algorithm are plotted again, as is the fractional deviation with respect to the mean of the two estimates. Similarity of both estimates, which is a necessary condition to get reliable results, is generally observed. Sporadic deviations (e.g., near observation 3450) are above-mentioned cases of "bad" convergence.

Another convenient way to globally characterize the results is to analyze the correlation between the $\langle R \rangle$ results over the 1601 observations for different pairs of algorithms using scatterplots. Such plots are shown in Fig. 13. For each case, the correlation coefficient ρ between $\langle R_1 \rangle$ and $\langle R_2 \rangle$ and the standard deviation (SD) relative to the mean of the two estimates are indicated in the legend. The line figuring out a hypothetical linear best fit to the results is also plotted.

Results at K_a band (Fig. 13a) illustrate the extent of the dynamic range over which kZS_K compensates for attenuation effects, while ZR_K saturates rapidly and underestimates the rainfall as soon as $\langle R \rangle$ exceeds about 1 mm h^{-1} in the present case. For low attenuation, convergence of both results toward the same values underlines the stability of kZS_K and its complementarity with $Z-R$. The same effect is observed for kZS_X (Fig. 13b), but the threshold over which ZR_X is negatively biased is increased to about 12 mm h^{-1}. The kZS_X and kZS_K results (Fig. 13c) are in fair agreement except for low rain rates (<10 mm h^{-1}), where kZS_X tends to produce lower estimates. An agreement between kZS_K and DF algorithm results (Fig. 13d) is acceptable, although significant scatter is observed. Indeed, agreement is not expected to be perfect since the DF algorithm is potentially able to perform better attenuation corrections than kZS algorithm except for some "bad convergence" cases alluded to earlier.

Finally, Fig. 14 shows several reconstructions of a 2D cross section of the rain rate from various algorithms within a part of the precipitating system. The selected part of the system corresponds to 201 observations (observations 2800 to 3000), or about 16 km in length. The rain-rate structures were drawn from gridded R-profiles results with a vertical resolution of 300 m, and an "equivalent" along-track resolution of 640 m using running mean over eight contiguous observations.

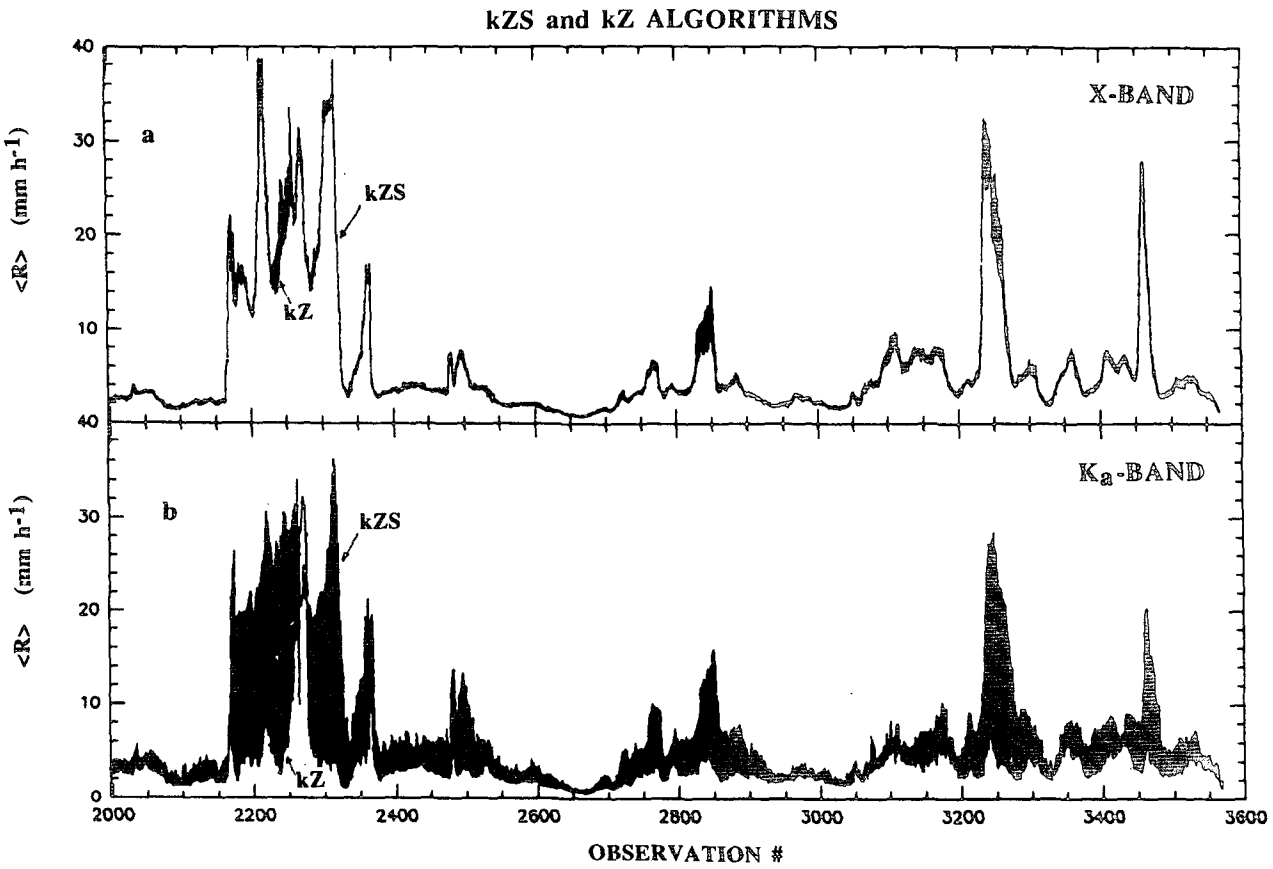

FIG. 10. Same as in Fig. 9 but for the rain estimates provided by the *kZS* and *kZ* algorithms, (a) at X band and (b) at K_a band.

Results from ZR_X (Fig. 13a) point out well-defined rain structures with a rain-cell core ($R_{max} \approx 9$ mm h^{-1}) centered at abscissa $x = 4$ km and a brightband peaking aloft near 3-km altitude, in the presence of moderate PIA effects. Almost all the observed structure are scratched in ZR_K estimate (Fig. 13b), owing to uncorrected PIA effects severely increasing deep in the rain. Attenuation corrections produced by kZS_X (Fig. 13c) and kZS_K (Fig. 13d) lead to fair recoveries of rain-rate patterns ($R_{max} \approx 15-18$ mm h^{-1}), especially at X band, with brightband peak much weaker at K_a band than at X band. The DF algorithm results yield the most detailed structures in rain ($R_{max} \approx 18$ mm h^{-1}) and in the melting region. Below 2-km altitude, and for abscissas between 2 and 4 km, the recovered 2D rain structure combines some local features obtained in kZS_X and kZS_K results, respectively. Let us recall that the *kZS* algorithm is constrained by surface echo measurements, while the DF algorithm does not make an explicit use of such additional measurements. Use of K_u band (near 14 GHz), or K band (near 24 GHz), is more commonly envisioned for spaceborne radars, such as TRMM radar at K_u band (Simpson et al. 1988). Results of $Z-R$ algorithm would be intermediate from those obtained at X and K_a bands, while the SF and DF algorithms, correcting for the involved PIAs, would likely yield similar kinds of results. For the DF algorithm, however, some features in the results may more specifically depend on the selected frequency pair, as suggested in MA94.

5. Simulation of nonuniform beam-filling effects

NUBF effects induced by rain-rate gradients within the radar beamwidth may be a significant source of bias in rain retrieval from spaceborne radar measurements. Very few studies have used real data precipitation fields to simulate such effects. Examples of works involving simulated spatial rain structures, such as models of rain cell defined on theoretical basis or derived from observed rainfall statistics, are more numerous (e.g., Goldhirsh and Walsh 1982; Testud et al. 1992; Amayenc et al. 1993; among others). These approaches allow an extended choice of simulation conditions but they are limited because realistic rain-rate distributions at various space scales are difficult to model. Two main ways may be followed to study NUBF effects taking into account actually observed rain structures.

A first way is to use precipitation fields derived from radar observations at nonattenuating frequencies. Na-

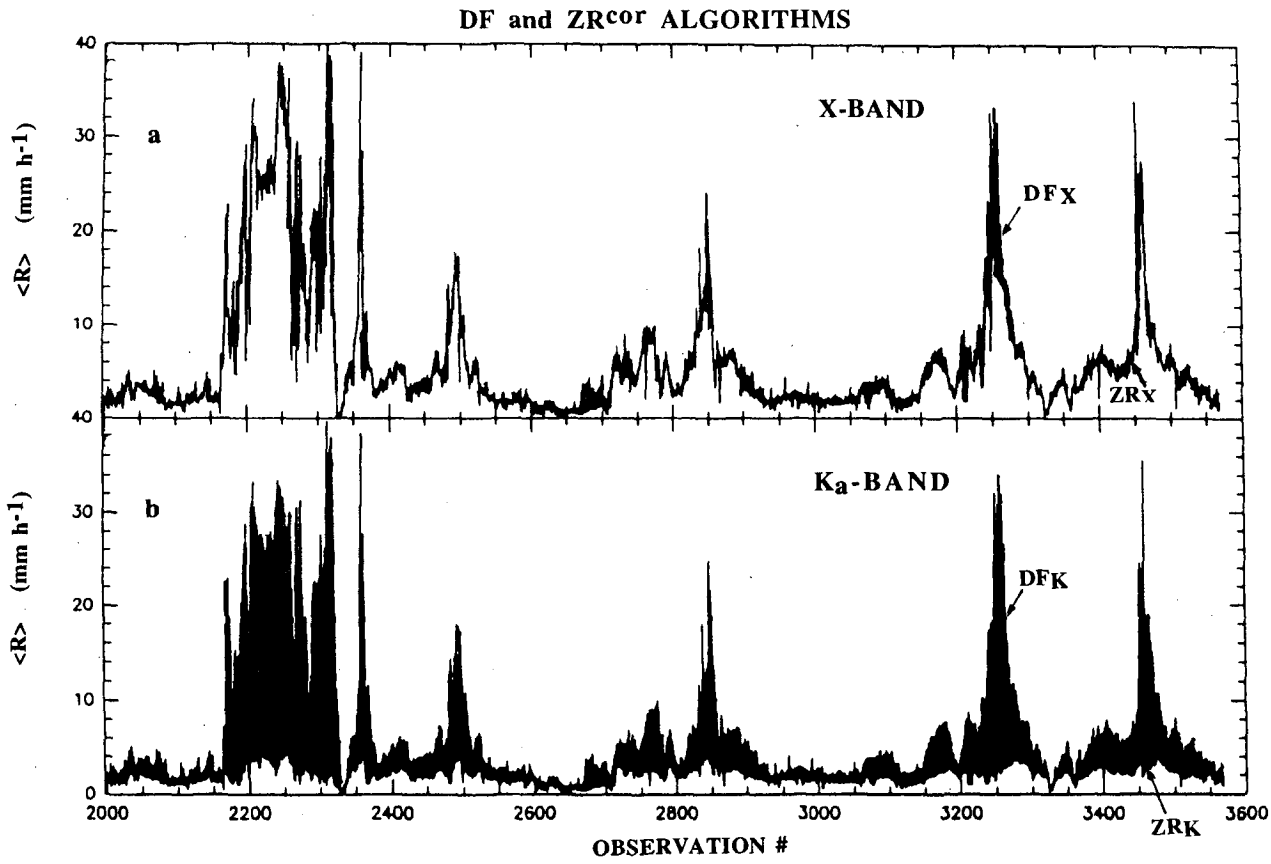

FIG. 11. Same as in Fig. 9 but for the two rain estimates provided by the DF algorithm, (a) at X band and (b) at K_a band, and for the rain estimate provided by the corrected Z^{cor}–R algorithm at each frequency.

kamura (1991) used a 1D time series of X-band radar measurements in Japan at a slant range of 2 km (1-km altitude). He assumed no height variation of the rain rate to produce a 2D rain field within an equivalent vertical plane. Then he used this rain field to simulate effects of NUBF in spaceborne radar measurements for different cross-range resolutions of a nadir-pointing radar beam and for several rain retrieval algorithms.

A second way is to use airborne radar observations simulating spaceborne measurements at attenuating frequencies. This is the method used in the present paper. Let us recall, however, that most conditions of the simulation are inherently attached to the measurements characteristics. Here results refer to the frequencies 10 and 35 GHz and to near-nadir beam incidence over ocean. In addition, since no acrosstrack information is available in the data, study of NUBF effects may be performed in 2D frame only.

a. Simulation conditions

1) METHOD AND DATA FOR BEAM AVERAGING

As explained in section 3b, the radar provides a nearly vertical cross section of the overflown rainy system. The sampling step is $\delta x \approx 80$ m in the alongtrack direction, denoted x. Every observation is obtained with a cross-range resolution $L_0 \approx 1$ km near the surface, equivalent to about 12 observations, and $L_0 \approx 0.5$ km at 5.6-km height (half the mean flight altitude) equivalent to about 6 observations. Thus, for each range gate, we are facing the following situation.

(i) Every genuine radar measurement may include some beam-averaging effect at "L_0 scale" involving weighted contribution of horizontal rain structures within an along-track distance interval $\pm L_0/2$, equivalent to ± 6 observations next to the surface, on each side of the measurement in question.

(ii) There is a large overlap from every observation to the next one.

(iii) Nearly independent observations corresponding to contiguous footprints, according to a sampling interval $L_0 \approx 1$ km, are obtained every 12 observations next to the surface.

Our purpose is to use this configuration to infer NUBF effects for cross-range resolutions $L > L_0$. Though NUBF effects are likely small at L_0 scale, the small sampling step ($\delta x \ll L_0$) prevents us from con-

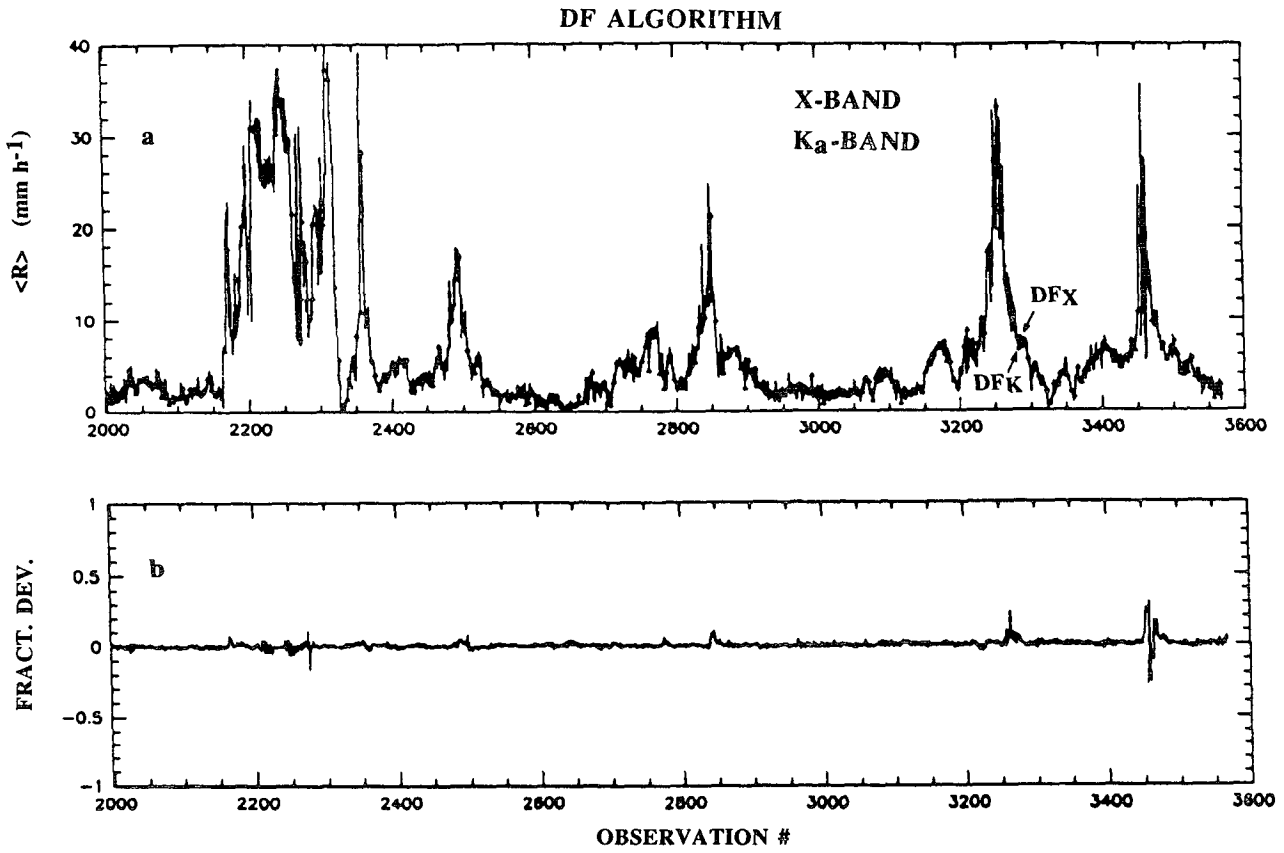

FIG. 12. Same as in Fig. 11 but (a) for the two rain estimates provided by the DF algorithm and (b) for their fractional deviation with respect to the mean.

sidering that radar measurements for successive observations are independent. Thus, we cannot compute a simple average, as if data were obtained with resolution δx, to get beam-averaged quantities for $L > L_0$. In fact, a correct simulation of NUBF effects at "L scale" should first involve a deconvolution of beam-averaging at L_0 scale to get measurements at "δx scale," then a new beam-averaging at L scale, for each altitude. Such a deconvolution, however, which would require an accurate knowledge of the radar beam gain function, is hard to conceive in the presence of path attenuation. Besides, it is generally unstable and vulnerable to noise. Thus, we looked for a more simple approach while assuming the following "idealized" conditions, which fit rather well to the observation.

(i) Measurements are obtained with a constant aircraft flight altitude and a nadir-pointing radar beam.

(ii) Resolution L_0 is taken constant with range and is equal to the value (1 km) near the surface.

(iii) The selected values $L = 2$, 3, and 4 km, also assumed constant with range, are typical of those actually envisioned for spaceborne radars; $L = 4$ km is close to the TRMM radar resolution at nadir.

(iv) The gain function of the simulated radar beam is Gaussian shaped.

(v) NUBF effects are mostly produced by along-track rain structures within the $\pm L/2$ distance interval and neglected in the acrosstrack direction.

The beam-averaged measurements at L scale were performed by a combining beam-averaged measurements at L_0 scale according to

$$X_{mL_0}(N_0) = \sum_{n=N_0-6m}^{n=N_0+6m} X_{L_0}(n)\left[\frac{W_G^2(n)}{P_w}\right] g(n - N_0), \tag{4}$$

where X is the averaged quantity at a given range (see below), X_L denotes beam-averaged value of X at L scale, $m = L/L_0$ refers to beam-averaging at "mL_0 scale," that is, L scale, N_0 is the reference observation number of the averaged quantity, $g(n - N_0) = 1$ for $(n - N_0) = 6k$ (k is an integer) and $= 0$ otherwise, W_G is the weighting factor of a Gaussian-shaped beam gain function given by

$$W_G(n) = \exp\left\{-4(\ln 2)\left[\frac{(n - N_0)\delta x}{L}\right]^2\right\}, \tag{5}$$

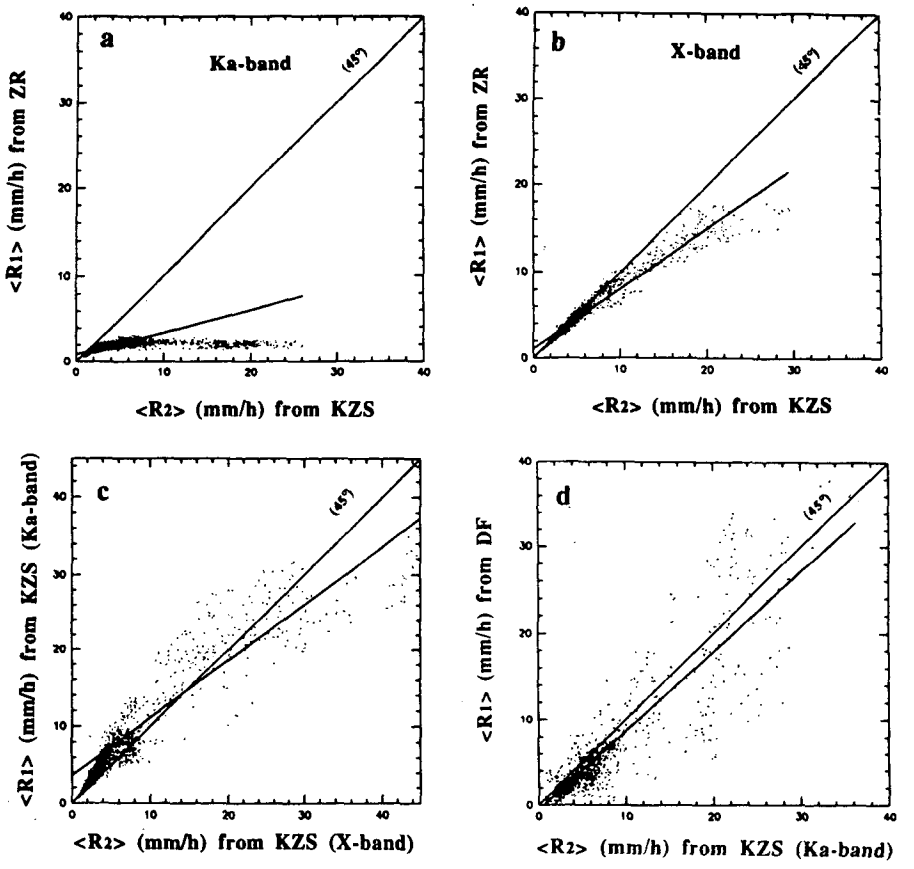

FIG. 13. Scatterplots of mean rain-rate estimates (average over a 2.5 km depth above the surface) $\langle R_1 \rangle$ versus $\langle R_2 \rangle$ computed from 1601R profile pairs (observations 2000–3600 on 1 November 1988) recovered from various algorithms. The involved algorithms for $\langle R_1 \rangle$ and $\langle R_2 \rangle$ are (a) Z–R versus kZS at K_a band (ρ = 0.825, SD = 70%); (b) Z–R versus kZS at X band (ρ = 0.976, SD = 14%); (c) kZS at K_a band versus kZS at X band (ρ = 0.902, SD = 29%); (d) DF versus kZS at K_a band (ρ = 0.902, SD = 41%). The bisectrix (45° line) and the linear regression line best fitting the data are also indicated for each case.

$\delta x = L_0/12$ ($\approx$80 m), and P_W is a normalizing factor of the gain function, such as $\Sigma\, W_G^2/P_w = 1$, given by

$$P_W = \sum_{n=N_0-6m}^{n=N_0+6m} W_G^2(n) g(n - N_0). \qquad (6)$$

The scheme for beam-averaging using (4) is illustrated in Fig. 15. Beam-averaging at L scale is performed by using beam-averaged measurements at L_0 scale with a step $L_0/2$. This value was chosen as a tradeoff between the following two extremes cases: (i) a step L_0, for contiguous measurements at L_0 scale, which could lead to lose some rain structures contributing to the beam filling; (ii) a step δx that would risk overaveraging rain structures, which would contribute to the beam filling. The method actually performs a 2D simulation of beam averaging within along-track–vertical space frame. In genuine data, the dimension of the "circular" 3-dB footprint is L_0 = 1 km. In the simulations, the "equivalent" dimensions of the 3-dB footprint are L_0 = 1 km across-track and L = 2, 3, or 4 km along-track, respectively.

We used the same dataset of 1601 observations, as in section 4d. For every selected observation N_0, we performed beam averaging at L scale of the range-gated received powers, including rain and surface returns at each frequency. In regions where signal was not detected, we left the noise to be summed up in the averaging process. By calculating the involved quantities at the "genuine" L_0 scale, that is, using (4) to recalculate X_{L_0} and comparing with the original results, we verified that the procedure did not induce bias due to some overaveraging effect. The σ^0 model outside rain was found to change by less than 0.2 dB at both frequencies for L = 2, 3, or 4 km, likely as a result of low variability in σ^0 at L_0 scale.

2) TESTS USED FOR ANALYZING NUBF EFFECTS

The sound nature of NUBF effects and the way they may be characterized have to be discussed. In essence,

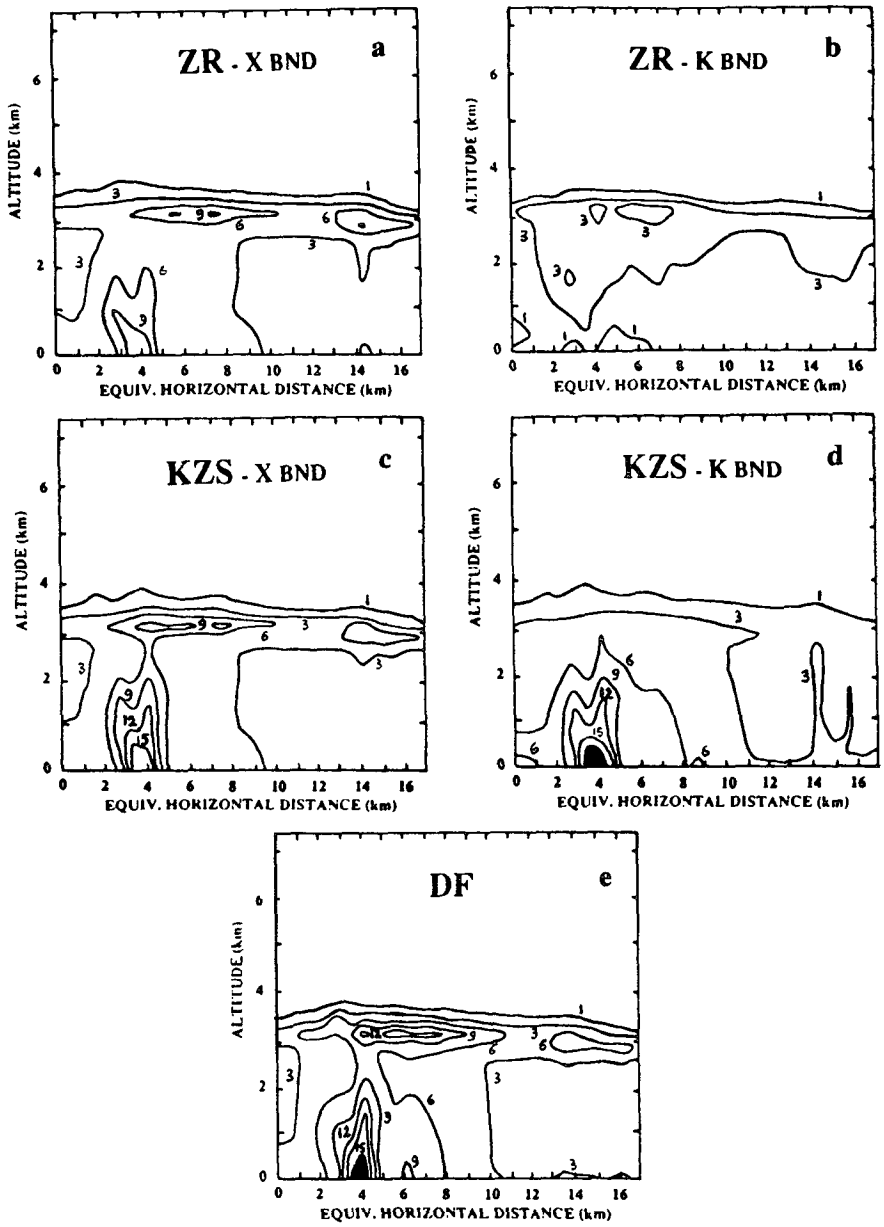

FIG. 14. Vertical cross sections (altitude versus the equivalent horizontal distance) of rain-rate structures reconstructed from the results of various range-profiling algorithms: (a) Z–R algorithm at X band, (b) Z–R algorithm at K_a band, (c) kZS algorithm at X band, (d) kZS algorithm at K_a band, and (e) DF algorithm. For each case, the results involve 201 contiguous recovered R profiles (observations 2800–3000 on 1 November 1988) at nearly vertical incidence.

given an algorithm and a cross-range resolution L, such effects refer to possible difference between the retrieved rain rate R_L and the "true" mean rain rate R_L^* averaged over L, which is the quantity actually expected to be retrieved.

When using theoretical rain models, it is possible to compute directly R_L^*. Analytical results and numerical simulations with kZS and kZ algorithms (Testud et al. 1992; Amayenc et al. 1993) showed that R_L generally underestimates the "true" mean rain rate R_L^*, owing to NUBF effects increasing with L. From simulations with real data, Nakamura (1991) found that either underestimation or overestimation effects, increasing with L, may occur depending on the involved algorithm.

When using real data from airborne radar, R_L^* is not known since the available rain-rate estimate R_L is de-

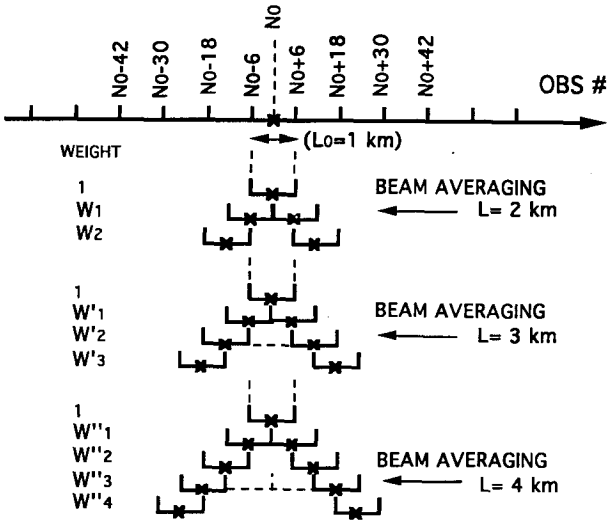

FIG. 15. Schemes used to simulate beam averaging for the selected 3-dB cross-range resolutions L = 2, 3, or 4 km from the genuine measurements with 3-dB cross-range resolution L_0 = 1 km. All schemes refer to observation N_0. Crosses (×) figure out the observations involved in the procedure. The normalized weighting factors, indicated qualitatively on the left-hand side, identify with the term W_0^2/P_w in Eq. (4); they correspond to a Gaussian-shaped gain function for a cross-range resolution L and apply to the involved observations on the same line.

rived from the results of the algorithms themselves. Given an algorithm, it is, however, possible to compare the rain rates R_L for different values of L. But if R_{L_0} is taken as reference, there is no theoretical reason to expect that similar characteristics be obtained by comparing R_L (for $L > L_0$) and R_{L_0} or R_L and R_L^*. A way to improve the conditions of comparison is to look for an estimate of R_L^* elaborated from R_{L_0}, which is the only available experimental quantity. Accordingly, the true mean rain rate R_L^* was approximately computed from a weighting average of contiguous R_{L_0} values over the cross-beam resolution L in question for every reference observation N_0, according to the general scheme

$$R_L^*(N_0) = \frac{1}{m} \sum_{n=N_0-6(m-1)}^{n=N_0+6(m-1)} R_{L_0}(n) h(n - N_1), \quad (7)$$

where $N_1 = N_0 - 6(m - 1)$, $L = mL_0$ with m = 1, 2, 3, 4, and $h(n - N_1) = 1$ for $(n - N_1) = 12k$ (k is integer of at least 0) and = 0 otherwise.

Equation (7) verifies $R_L^*(N_0) = R_{L_0}(N_0)$ for $L = L_0$. As an example for $L = 3L_0$, the computation scheme is

$$R_L^*(N_0) = \frac{1}{3}[R_{L_0}(N_0 - 12) + R_{L_0}(N_0) + R_{L_0}(N_0 + 12)]. \quad (8)$$

The R_L^* estimate depends on the considered algorithm. This is, however, not very penalizing because R_{L_0}, even possibly different for the various algorithms, is weakly affected by NUBF. Also, it can be verified that for every algorithm the mean value $[R_L^*]_N$ of R_L^* over a set of N contiguous observations is independent of L and nearly equal to the mean value of R_{L_0}; that is,

$$[R_L^*]_N \approx \frac{1}{N} \sum_{n=1}^{n=N} R_{L_0}(n), \quad (9)$$

provided that $N \gg 6(m - 1)$. A small difference may appear, resulting from edge effects.

In the following, we present results of the comparison between R_L (the 3-dB beam-averaged rain rate at L scale) and either R_{L_0} (the 3-dB beam-averaged rain rate at L_0 scale) or R_L^* (the estimated true mean rain rate at L scale) for every algorithm. The former comparison points out bulk effects of beam-averaging, while the latter one characterizes intrinsic effects of NUBF.

b. *Analysis of results*

We characterized beam-averaging effects in the height-averaged rain rates $\langle R_L \rangle$ computed from the R_L profiles recovered from the algorithms over the 1601 observations of the dataset. The height average was still performed over the first 2.5 km above the surface. Results are focused on *kZS*, DF, and Z–R algorithms.

An example of simulated results, for L = 3 km, are displayed in Fig. 16 for Z_X–R and kZS_X and for Z_K–R and kZS_K. They can be compared with those of Fig. 9 at L_0 scale (1 km). Similar results, for L = 3 km, but referring to the two rain rate estimates (at X and K_a band) of the DF algorithm, are plotted in Fig. 17, along with results obtained from Z^{cor}–R relation at each frequency. They can be compared with those of Fig. 11 at L_0 scale. Beam-averaging effects are characterized by the following features in $\langle R_L \rangle$, compared with $\langle R_{L_0} \rangle$:

(i) the "small scale" space structures of the rain rate are smoothed out;

(ii) R_L generally decreases when L increases for heavy rain and remains nearly unchanged for low rain; and

(iii) the most important changes are observed for regions that include large rain-rate gradients over a series of contiguous observations where local increase of $\langle R_L \rangle$ with L may occasionally take place.

These features are valid for *kZS* and DF algorithms as well as for the Z–R and Z^{cor}–R algorithms results; they strengthen with L values increasing from 2 to 4 km (not shown). It is not surprising that increasing the averaging scale L produces a decrease of $\langle R_L \rangle$. This effect is more pronounced for high rain rates that correspond to convective rain with nonhomogeneous structures at small scale than for low rain rates that correspond to more stratiform rain. Intrinsic NUBF effects, however, are present only if R_L differs from $\langle R_L^* \rangle$ at L scale.

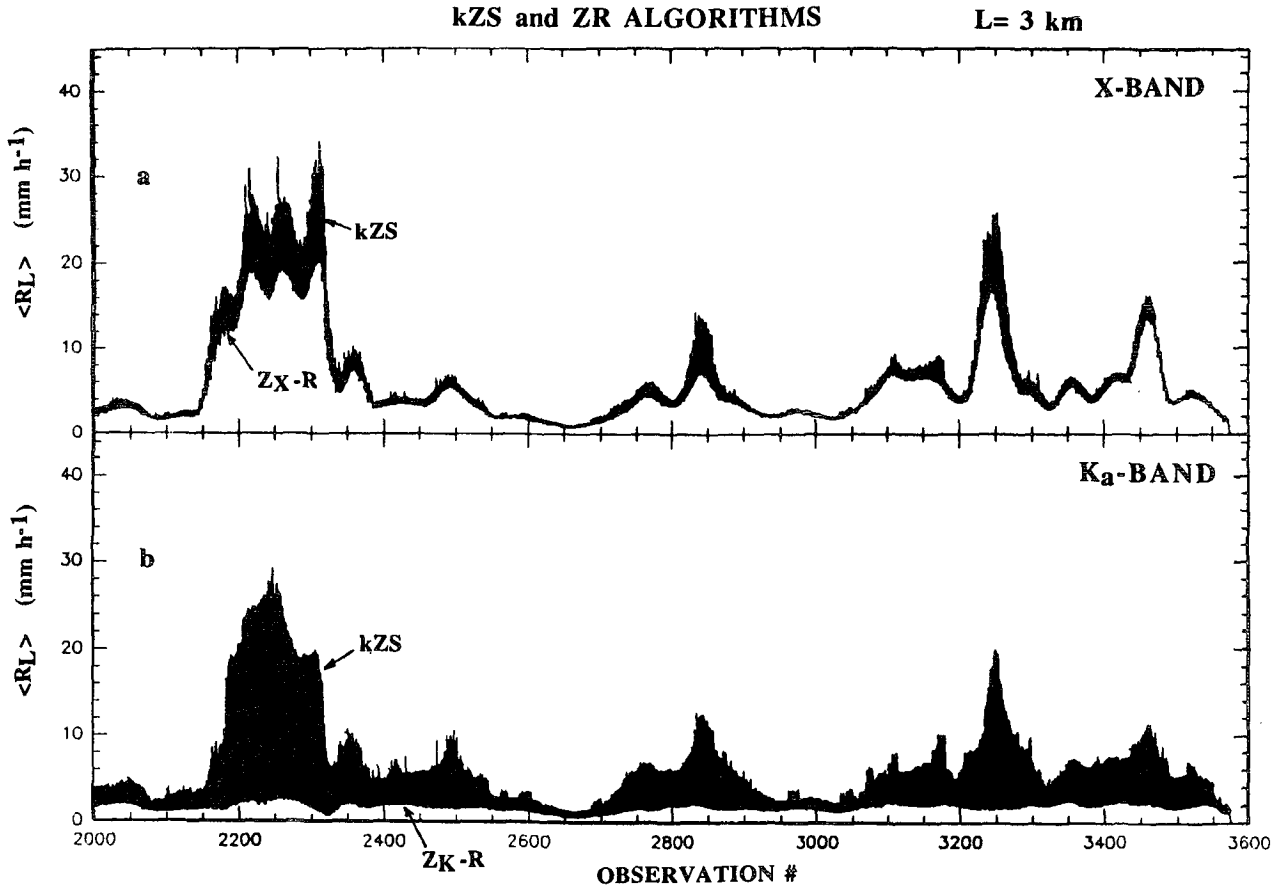

FIG. 16. Mean rain rates $\langle R_L \rangle$ (average over a 2.5-km depth above the surface) computed from 1601 profiles (observations 2000–3600 on 1 November 1988) retrieved from *kZS* and *Z–R* algorithms with a simulated cross-range resolution L = 3 km: (a) at X band and (b) at K_a band. For each panel, a positive (negative) difference between *kZS* and *ZR* algorithms results is characterized by a black (blank) area. See Fig. 9 for comparison with results at the original resolution L_0 = 1 km.

The correlation coefficient ρ_1 and the relative rms deviation $\sigma_{1\text{rms}}$ between $\langle R_L \rangle$ and $\langle R_{L_0} \rangle$ on one hand and ρ_2 and $\sigma_{2\text{rms}}$ between $\langle R_L \rangle$ and $\langle R_L^* \rangle$ on the other hand, as function of L, are listed in Table 4 for the kZS_X, kZS_K, and DF algorithms. The rms deviations, for the N = 1601 observations were computed as

$$\sigma_{1\text{rms}} = 100\left\{\frac{1}{N}\sum_{n=1}^{n=N}\left(\frac{\langle R_L(n)\rangle - \langle R_{L_0}(n)\rangle}{\langle R_{L_0}(n)\rangle}\right)^2\right\}^{1/2} \tag{10}$$

$$\sigma_{2\text{rms}} = 100\left\{\frac{1}{N}\sum_{n=1}^{n=N}\left(\frac{\langle R_L(n)\rangle - \langle R_L^*(n)\rangle}{\langle R_L^*(n)\rangle}\right)^2\right\}^{1/2}. \tag{11}$$

Results of Table 4 show that for every algorithm the rms deviation due to specific effects of NUBF ($\sigma_{2\text{rms}}$) is greater than the rms deviation due to effects of beam-averaging ($\sigma_{1\text{rms}}$), both increasing with L. A significant part of the observed deviations corresponds to bias in R_L compared with either R_L^* or R_{L_0}.

Finally, the impact of NUBF effects may be synthesized by comparing the averaged values of $\langle R_L \rangle$ and $\langle R_L^* \rangle$ over the entire dataset. This kind of computation is important since a major goal for future spaceborne missions carrying rain radar is to provide rain-rate estimates at large scale. Let us recall that the 1601 observations are equivalent to an alongtrack length of about 128 km. The mean rain rates over the dataset, denoted by the square brackets, were computed as

$$[\langle R_L \rangle] = \frac{1}{N}\sum_{n=1}^{n=N}\langle R_L(n)\rangle \tag{12}$$

$$[\langle R_L^* \rangle] = \frac{1}{N}\sum_{n=1}^{n=N}\langle R_L^*(n)\rangle. \tag{13}$$

The variations of $[\langle R_L \rangle]$ versus L for the various algorithms are plotted in Fig. 18a. The $[\langle R_{L_0} \rangle]$ estimates are close to each other for the "attenuation" algorithms. For L ranging from 2 to 4 km, all results stand within a 12% margin. The ZR_X algorithm results, moderately affected by uncorrected attenuation effects,

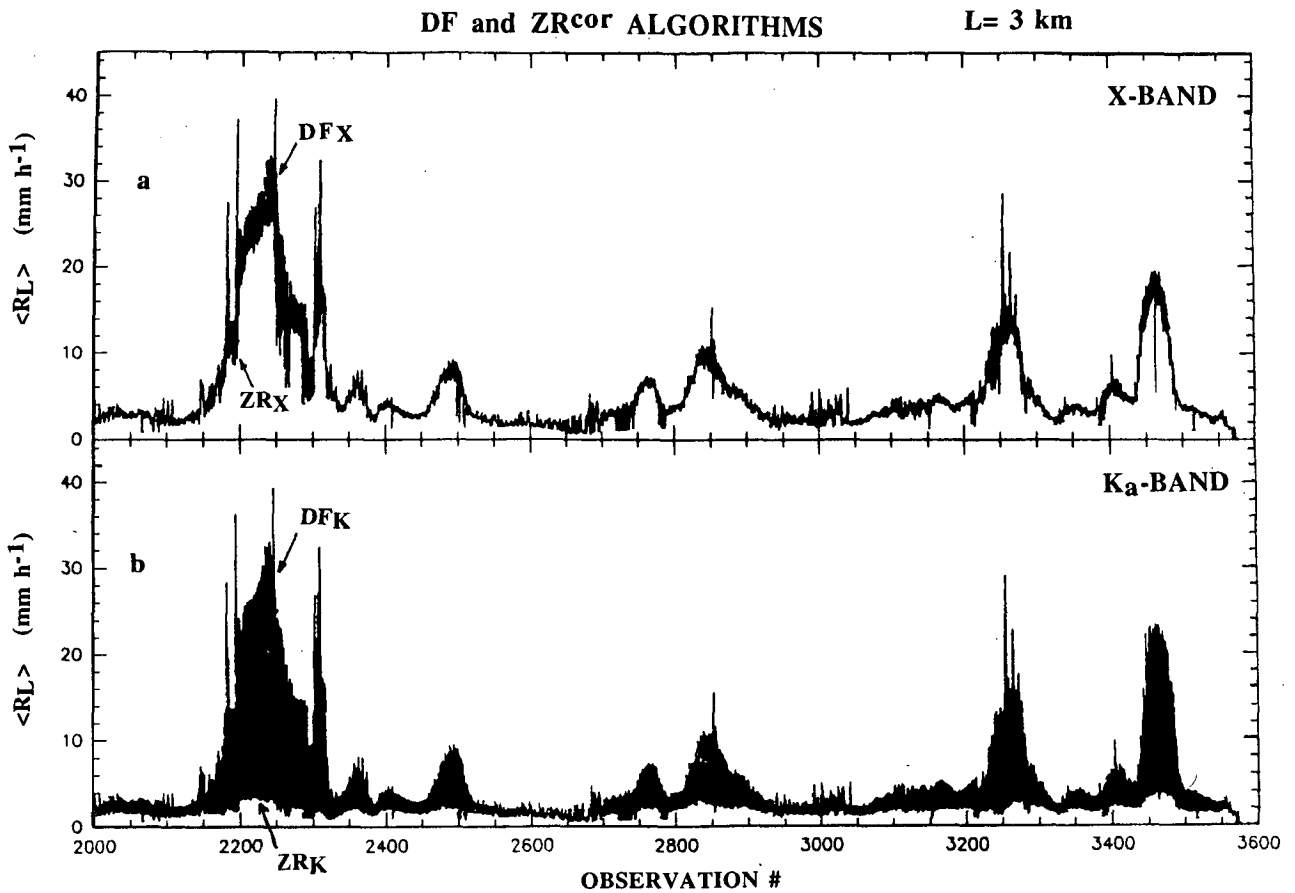

FIG. 17. Same as in Fig. 16 but for the DF algorithm and the "corrected" Z^{cor}–R algorithm with a simulated cross-range resolution L = 3 km (a) at X band and (b) at K_a band. See Fig. 11 for comparison with results at the original resolution L_0 = 1 km.

are 20%–30% lower. The ZR_K algorithm results, uncorrected for large PIA effects, are about 75% lower.

The variations of $[\langle R_L\rangle][\langle R_L^*\rangle]^{-1}$ versus L, characterizing mean bias due to NUBF for the same algorithms, are plotted in Fig. 18b. Term ZR_X, although it underestimates the rain rate, is almost unbiased (less than 2%) by NUBF effects. The same is true for ZR_K results (not shown). For kZS_X, low positive bias due to NUBF slightly increases with L from +2% for L = 2 km to +4% for L = 4 km. For kZS_K, negative bias due to NUBF increases with L from −8% for L = 2 km to −12% for L = 4 km. The DF algorithm results also indicate that negative bias due to NUBF increases with L from −12% for L = 2 km to −15% for L = 4 km. For every "attenuation" algorithm, the systematic difference (or bias) at L scale between $[\langle R_L\rangle]$ and $[\langle R_L^*\rangle]$ is much lower than the total rms deviation (σ_{2rms}) between the two quantities (cf. Table 4). This is because the random part of the deviation cancels out when averaging over the entire dataset. In addition, if $[\langle R_{L_0}\rangle]$ instead of $[R_L^*]$ was used for comparison with $[\langle R_L\rangle]$, the results would be nearly identical since $[\langle R_L^*\rangle] \approx [\langle R_{L_0}\rangle]$ according to (9). Thus, at large scale, bias due to beam-averaging identifies with bias due to intrinsic NUBF effects.

Results of the intrinsic NUBF effects study by Nakamura (1991), though performed for different conditions, exhibit bulk features comparable to those shown here: they produce positive bias in the Z–R method and negative bias in attenuation algorithms except for a special case of the standard DF approach; all biases increase with the averaging spatial scale.

Analytical study of NUBF for SF algorithms (Amayenc et al. 1993) showed that the two main competing biasing effects were a bias B_1, due to the "concavity of the exponential PIA function" in cross-range averaging, which produces underestimation of the rain rate, increasing with the PIA, and a bias B_2, due to the "nonlinearity of $Z = \alpha k^\beta$ relations" used in the algorithms processing, which produces underestimation or overestimation of the rain rate, increasing with β. The observed features for SF algorithms are in bulk agreement with these predictions. At X band, bias B_2 likely compensates for, or dominates, bias B_1 owing to low PIA values and produces a final positive low bias. At K_a band, bias B_1 dominates bias B_2 owing to much larger

TABLE 4. Correlation coefficient ρ_1 (ρ_2) and relative rms deviation $\sigma_{1\text{rms}}$ ($\sigma_{2\text{rms}}$) between $\langle R_L \rangle$ and $\langle R_{L_0} \rangle$ ($\langle R_L \rangle$ and $\langle R_L^* \rangle$) for the range-profiling attenuation algorithms kZS_X, kZS_K, and DF, respectively, and for different simulated cross-range resolution L. Here R_L is the simulated beam-averaged rain rate; R_L^* is an estimate of the true mean rain rate (averaged over L). The genuine resolution of the radar beam is L_0 = 1 km. The angle brackets stand for a height average of the involved quantity over a 2.5-km depth above the surface. Results refer to the entire dataset (observations 2000–3600).

		Cross-range resolution		
Algorithm	Parameter	L = 2 km	L = 3 km	L = 4 km
kZS_X	ρ_1	0.981	0.976	0.968
	$\sigma_{1\text{rms}}$ (%)	13	14	16
	ρ_2	0.957	0.920	0.882
	$\sigma_{2\text{rms}}$ (%)	21	28	33
kZS_K	ρ_1	0.972	0.956	0.947
	$\sigma_{1\text{rms}}$ (%)	18	22	25
	ρ_2	0.947	0.931	0.916
	$\sigma_{2\text{rms}}$ (%)	20	25	28
DF	ρ_1	0.935	0.888	0.886
	$\sigma_{1\text{rms}}$ (%)	30	34	36
	ρ_2	0.909	0.866	0.862
	$\sigma_{2\text{rms}}$ (%)	34	38	40

PIA and produces a final negative bias. Results for the DF algorithm do not point out any superiority over the SF counterparts. This would not necessarily be the case for other frequency pairs.

The present results (Fig. 18b) also indicate that ranking of the algorithms with respect to their sensitivity to NUBF in decreasing merit order would yield first ZR_K, then ZR_X, and finally the "attenuation" algorithms kZS_X, kZS_K, and DF, in that order. This is actually a puzzling result since it somewhat weakens the advantage of attenuation algorithms over $Z-R$ methods and of the DF approach over the SF counterparts to perform corrections of various scaling errors (cf. MA94, and section 4). The experimental data likely include such types of error and low NUBF effects at L_0 scale. Algorithms performances must be evaluated by comparing sensitivity to all causes of error among which possible impact of NUBF does not necessarily dominate. Attenuation algorithms, though possibly more biased by NUBF, can still be preferred to $Z-R$ methods that are almost unbiased by NUBF but ignore correction of path attenuation.

6. Final discussion and conclusions

Dual-frequency airborne radar data were used to study the performances of several SF algorithms and a DF algorithm aimed at profiling the rainfall rate versus range from a downward-looking spaceborne radar, as described in Part I (MA94). Such data mimic spaceborne radar measurements, including realistic error sources, such as an offset in the radar calibration, DSD variability, and σ^0 fluctuations. Most conditions, however, are attached to the characteristics of the experiment: 10 and 35 GHz and near-nadir beam pointing in the present case.

Rain retrievals were performed for stratiform and convective rain cases. In absence of "external" measurements to validate the rain estimates, we primarily checked the self-consistency of the results. The SF algorithms produce more or less scattered results depending on their own sensitivities to uncorrected scaling errors. Improvement of the SF approach stability by using surface echo measurements as a constraint on the total PIA (*kZC* and *kZS* algorithms) was confirmed. The *kZS* algorithm, integrating from the surface, pro-

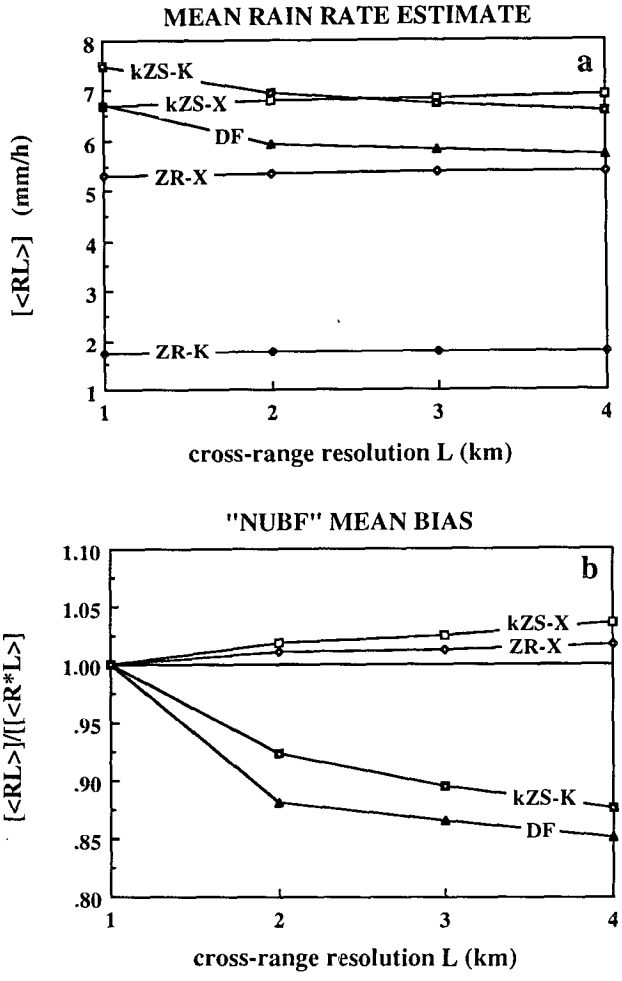

FIG. 18. Mean values over the entire dataset (observations 2000–3600), denoted by the square brackets of (a) $[\langle R_L \rangle]$ and (b) the ratio $[\langle R_L \rangle][\langle R_L^* \rangle]^{-1}$, as function of the simulated cross-range resolution L. Results are shown for the range-profiling attenuation algorithms kZS_X, kZS_K, and DF, respectively. Results for ZR_X, and ZR_K algorithms are also plotted for comparison. Here R_L is the simulated beam-averaged rain rate; R_L^* is an estimate of the true mean rain rate (averaged over L). Term L_0 = 1 km is the genuine resolution of the radar beam. The angle brackets stand for the height average of the involved quantity over a 2.5-km depth above the surface.

duces generally the more reliable results, that is, the most similar at X band and K_a band within the detectable rain rate range, and fairly converges toward $Z-R$ estimate for low PIA. The *kZC* algorithm works correctly for large PIA but produces scattered results at low PIA. Conversely, the *kZ* algorithm, processing rain echoes only, works correctly at low PIA (<3 dB) but often collapses for large PIA (>3 dB). The *kZN* algorithm yields coherent results but may be penalized in the presence of significant height gradient of the rain rate near the surface.

The correlation between the attenuation coefficients at both frequencies, which forms the theoretical basis of the DF algorithm, was experimentally verified. Results from the DF algorithm are thought to be more reliable than the SF counterparts since they are globally corrected for scaling errors. Besides, the radar calibration correction derived from the DF algorithm results may be used to improve results of the $Z-R$ method, at least for low PIA. Results of rain profiling from *kZS* and DF algorithms allowed us to reconstruct coherent 2D raincell structures in a part of the observed rainy system.

The frequencies involved in the airborne radar data call for some comments. Use of radar data at X band and K_a band has some drawbacks for the application of SF algorithms. At X band, low attenuation (for $R < 5$ mm h^{-1}) may be masked by the variability in the σ^0 estimate. At K_a band, large attenuation (for $R > 20$ mm h^{-1}) can prevent detection of signal deep in the rain before the surface range. The DF approach, however, benefits by large differential attenuation effects. Since algorithm performances are mainly driven by the PIA, results at K_u band and K band, more usually planned for future spaceborne radars, may be inferred from relevant frequency-dependent $k-R$ relations. The mean rain-rate threshold R_T above which "attenuation" algorithms should relay the $Z-R$ method to avoid negative bias in rain-rate estimates were found near 1 mm h^{-1} at 35 GHz and 12 mm h^{-1} at 10 GHz, respectively, for a 2.5-km rain depth. This threshold would be $R_T \approx 1.5$ mm h^{-1} at 24 GHz and ≈ 5 mm h^{-1} at 14 GHz, respectively. For constant rain rate, all thresholds correspond to a PIA ≈ 1 dB, which is a lower limit for a reliable application of "attenuation" algorithms using surface echo measurements. Future work will involve tests of algorithms using data gathered over the western Pacific Ocean during TOGA COARE (Webster and Lukas 1992) with the Airborne Rain-Mapping Radar (ARMAR) at K_u band (Durden et al. 1994) on board the DC8 aircraft of NASA.

The general features of the aforementioned results are in good agreement with previous works by other researchers who used similar datasets to test algorithms dedicated to rain profiling (Meneghini and Nakamura 1990; Kozu et al. 1991; Meneghini et al. 1992; Iguchi and Meneghini 1994). Though most numerical values are related to specific conditions of the experiment, the main conclusions applicable to other cases, also supported by results of Part I, are the superiority of "attenuation-compensating" over $Z-R$ methods to retrieve spatial structures or path averages of the rain rate, the primary control of the algorithm performances by the PIA amount in the merit–demerit balance, the benefit of using surface echo as a constraint to stabilize the SF algorithms over a large dynamic range, and the potential improvement brought by the DF approach over the SF counterparts to better correct scaling errors. Also, there is a promising way, initiated by Iguchi and Meneghini (1994), to investigate "hybrid" algorithms exploiting the well-identified complementary advantages of the various SF approaches.

The airborne radar measurements obtained with high cross-range resolution ($L_0 \approx 1$ km) were also used to simulate 2D beam-averaging effects and intrinsic NUBF effects for larger cross-range resolutions $L = 2$, 3, and 4 km in the alongtrack direction. Approximate computations of the relevant quantities were elaborated to point out both effects. Beam-averaging produces smoothing of small-scale rain-rate structures and bulk lowering of the rain rate as expected consequences of degrading the cross-range resolution. Intrinsic NUBF effects are characterized by deviations between the derived beam-averaged rain rate and the "true mean rain rate" over the beamwidth. They produce low positive bias, slowly increasing with L, for kZS_X and more important negative bias, increasing with L, for kZS_K and the DF algorithm. Impact of NUBF effects on mean rain-rate estimates at large scale (≈100 km), derived from attenuation algorithms, remains tolerable: the bias culminates near −15% to +2% for $L = 4$ km, depending on the involved algorithm. The main feature, in overall agreement with results of Nakamura (1991), is that NUBF effects produce overestimation of the rain rate in $Z-R$ methods and underestimation of the rain rate in attenuation methods as soon as PIA becomes significant. The magnitude of NUBF effects, however, is governed by the measurement geometry and the attenuation rate. Thus, the obtained numerical results are inherently attached to the conditions of the experiment. They would not necessarily be the same for other conditions referring to frequencies, beam incidences, and storm structures.

It should finally be emphasized that an objective ranking of the bulk merits of the various algorithms has to appreciate their own sensitivities to all types of scaling errors possibly present in the measurements, not only to the NUBF.

Acknowledgments. This study received financial support from the Centre National d'Etudes Spatiales (France), and Comité PATOM de l'Institut National des Sciences de l'Univers (France). Part of the study also received financial support from the European Space Agency under Grant ESTEC 10204/92/NL/NB(SC). We wish to thank Dr. R. Meneghini from

NASA/GSFC for providing us the airborne radar dataset.

APPENDIX

A Useful Expression to Estimate the PIA in the (r, r_s) Range Interval above the Surface

For the SF approach, a general expression of the two-way PIA factor $A(r, r_s)$ in a limited range interval (r, r_s) above the surface, assuming detectable rain signal down to the surface range r_s, may be derived from MA94 [see (17), with $r_d = r_s$], according to

$$A(r, r_s) = \left[1 + \left(\frac{y_g}{x_g}\right) S(r, r_s)\right]^{-\beta}, \quad \text{(A1)}$$

where $S(r_1, r_2)$, given by

$$S(r_1, r_2) = \int_{r_1}^{r_2} Z_{am}^{1/\beta}(s)\, ds, \quad \text{(A2)}$$

involves apparent reflectivity measurements (Z_{am}) within rain, and β is a coefficient of the $Z = \alpha k^{\beta}$ relation. The expressions for x_g and for $y_g = (1 - x_g)/S(r_0, r_s)$ depend on the involved algorithm (index g).

For *kZS* algorithm ($g = 3$), x_3 derived from MA94 [see (24), with $r_d = r_s$] is given by

$$x_3 = \frac{(A_{tm}\alpha\delta A_t\delta C)^{1/\beta}}{(A_{tm}\alpha\delta A_t\delta C)^{1/\beta} + \gamma S(r_0, r_s)}, \quad \text{(A3)}$$

where α is a coefficient of the $Z = \alpha k^{\beta}$ relation, A_{tm} is the total PIA measured from surface echo attenuation below rain, $S(r_0, r_s)$ is defined by (A2), and $\gamma = 0.46/\beta$. The terms δC and δA_t represent possible uncorrected scaling errors in the radar calibration constant C for rain echoes and in the A_{tm} estimate, respectively. They are defined as multiplying factors of the assumed value.

Combining (A1), (A2), and (A3) yields the following expression for the two-way PIA factor $A(r, r_s)$:

$$A(r, r_s) = \left[1 + \gamma \frac{S(r, r_s)}{(\alpha A_{tm}\delta A_t\delta C)^{1/\beta}}\right]^{-\beta}$$

$$= \left[1 + \left(\frac{0.46}{\beta}\right)\int_r^{r_s}\left(\frac{Z_{am}(s)}{\alpha A_{tm}\delta A_t\delta C}\right)^{1/\beta} ds\right]^{-\beta}. \quad \text{(A4)}$$

The $A(r, r_s)$ estimate, always positive, is obtained by integration between the surface range r_s and any range r. Thus, like the $k(r)$ profile, it is independent of the storm structure at ranges less than r. It remains, however, sensitive to errors δA_t that may arise from uncertainty in the σ^0 estimate due to effects of surface wind or drop impact over ocean, for example, and to uncertainty in the α coefficient due to DSD variability. The dependence on the β parameter, which appears essentially as a norm in (A4), is almost negligible.

Sensitivity of $A(r, r_s)$ to an error δC in the radar calibration referring to Z_{am} measurements in (A4), deserves further comment. The total PIA factor A_{tm} is derived from the ratio of surface echo powers measured outside rain as a "reference" and below rain at different times and/or locations. This involves two possible additional errors in the radar calibration C_s for surface echo measurements: δC_{s0} outside rain and δC_s below rain. Since the radar returns from rain and the surface below rain are obtained "simultaneously" for the same path, δC and δC_s cancel out in the Z_{am}/A_{tm} ratio of (A4). Thus, $A(r, r_s)$ may be considered as insensitive to error in the radar calibration *below rain* but sensitive to a calibration error δC_{s0} in surface echo measurements *outside rain* only. Term δC_{s0}, in turn, can be considered a part of the error in A_{tm}, thereby included in the bulk error δA_t. The same reasoning also applies to the $k(r)$ profile estimated from the *kZS* algorithm.

For a practical computation of $A(r, r_s)$ using (4), Z_{am} (A_{tm}) may be expressed as a function of returned power $P(r)$ from rain [$P_s(r_s)$ from the surface], and error terms may be neglected by taking $\delta A_t = \delta C = 1$, which yields finally

$$A(r, r_s) = \left[1 + \left(\frac{0.46}{\beta}\right) \times \int_r^{r_s}\left(\frac{P(r)r^2C_s\sigma^0}{P_s(r_s)r_s^2C\alpha}\right)^{1/\beta} dr\right]^{-\beta}, \quad \text{(A5)}$$

where σ^0 is the "reference" value of the surface backscattering coefficient.

REFERENCES

Amayenc, P., and M. Marzoug, 1992: A survey of algorithms studies developped at CRPE for range profiling of rain rate from a spaceborne radar. *Proc. Int. Workshop on the Processing and Utilization of the Rainfall Data Measured from Space,* Tokyo, Japan, Communications Research Laboratory, 289–294.

——, ——, and J. Testud, 1993: Analysis of cross-beam resolution effects in rainfall rate profile retrieval from a spaceborne radar. *IEEE Trans. Geosci. Remote Sens.,* **31,** 417–425.

Atlas, D., and C. W. Ulbrich, 1977: Path- and area-integrated rainfall measurement by microwave attenuation in the 1–3-cm band. *J. Appl. Meteor.,* **16,** 1322–133.

Durden, S. L., E. Im, F. K. Li, W. Ricketts, A. Tanner, and W. Wilson, 1994: ARMAR: An Airborne Rain-Mapping Radar. *J. Atmos. Oceanic Technol.,* **11,** 727–737.

Fujita, M., K. Okamoto, M. Masuko, S. Yoshikado, and K. Nakamura, 1985: Inference of rain rate profile and path-integrated rain rate by an airborne microwave rain scatterometer. *Radio Sci.,* **20,** 631–642.

Goldhirsh, J., and E. J. Walsh, 1982: Rain measurements from space using a modified Seasat-type radar altimeter. *IEEE Trans. Antenna Propag.,* **30,** 726–732.

Hitschfeld, W., and J. Bordan, 1954: Errors inherent in the radar measurement of rainfall at attenuating wavelengths. *J. Meteor.,* **11,** 58–67.

Iguchi, T., and R. Meneghini, 1994: Intercomparison of single frequency methods for retrieving a vertical rain profile from airborne or spaceborne radar data. *J. Atmos. Oceanic Technol.,* **11,** 1507–1516.

Kozu, T., 1991: Estimation of raindrop size distribution from spaceborne measurement. Ph.D. thesis, Kyoto University, 196 pp.

——, K. Nakamura, R. Meneghini, and W. Boncyk, 1991: Dual parameter rainfall measurement from space: A test result from an aircraft experiment. *IEEE Trans. Geosci. Remote Sens.*, **29,** 690–703.

Marshall, J. S., and W. M. K. Palmer, 1948: The distribution of raindrop with size. *J. Meteor.*, **5,** 165–166.

Marzoug, M., and P. Amayenc, 1991a: Experimental tests of an improved single frequency algorithm for rain rate profiling using airborne radar data. *Proc. 25th Int. Conf. on Radar Meteorology,* Paris, France, Amer. Meteor. Soc., 396–399.

——, and ——, 1991b: Improved range profiling algorithm of rainfall rate from a spaceborne radar with path-integrated attenuation constraint. *IEEE Trans. Geosci. Remote Sens.* (Special issue IGARSS'90), **GE-29,** 584–592.

——, and ——, 1992: A new class of dual-frequency algorithms for rain rate profiling from, a spaceborne radar: Principle and tests. *Proc. IGARSS'92,* Houston, TX, 1376–1379.

——, and ——, 1993: Algorithms for range profiling of rain rate from a spaceborne radar: Overall validation using airborne radar data. *Proc. 26th Conf. on Radar Meteorology,* Norman, OK, Amer. Meteor. Soc., 690–693.

——, and ——, 1994: A class of single- and dual-frequency algorithms for rain rate profiling from a spaceborne radar. Part I: Principle and tests from numerical simulations. *J. Atmos. Oceanic Technol.*, **11,** 1480–1506.

Meneghini, R., and T. Kozu, 1990: *Spaceborne Weather Radar.* Artech House, 199 pp.

——, and K. Nakamura, 1990: Range profiling of the rain rate by an airborne weather radar. *Remote Sens. Environ.*, **31,** 193–209.

——, J. A. Jones, and L. H. Gesell, 1987: Analysis of a dual-wavelength surface reference radar technique. *IEEE Trans. Geosci. Remote Sens.*, **21,** 34–43.

——, K. Nakamura, C. W. Ulbrich, and D. Atlas, 1989: Experimental tests of methods for the measurement of rainfall rate using an airborne dual-wavelength radar. *J. Atmos. Oceanic Technol.*, **6,** 637–651.

——, T. Kozu, H. Kumagai, and W. C. Boncyck, 1992: A study of rain estimation methods from space using dual-wavelength radar measurements at near-nadir incidence over ocean. *J. Atmos. Oceanic Technol.*, **9,** 364–382.

Nakamura, K., 1991: Biases of rain retrieval algorithms for spaceborne radar caused by nonuniformity of rain. *J. Atmos. Oceanic Technol.*, **8,** 363–373.

Okamoto, K., T. Ojima, S. Yoshikado, H. Masuko, H. Inomata, and N. Fugono, 1982: System design and examination of spaceborne microwave rain scatterometer. *Acta Astronaut.*, **9,** 713–721.

Simpson, J., R. F. Adler, and G. R. North, 1988: A proposed Tropical Rainfall Measuring Mission (TRMM). *Bull. Amer. Meteor. Soc.*, **69,** 278–295.

Testud, J., P. Amayenc, and M. Marzoug, 1992: Rainfall rate retrieval from a spaceborne radar: Comparison between single-frequency, dual-frequency, and dual-beam techniques. *J. Atmos. Oceanic Technol.*, **9,** 599–623.

Webster, P. J., and R. Lukas, 1992: TOGA-COARE: The Coupled Ocean–Atmosphere Response Experiment. *Bull. Amer. Meteor. Soc.*, **73,** 1377–1416.